NTNU

Norwegian University of
Science and Technology

SolarThermal Splitting of Water to Hydrogen with Co-doped-hercynite

Testing and Characterisation / Heat integration

Tor Olav Høva Erevik

Chemical Engineering and Biotechnology
Submission date: July 2016
Supervisor: Magne Hillestad, IKP
Co-supervisor: Erling Rytter, IKP

Norwegian University of Science and Technology
Department of Chemical Engineering

Solar Thermal Water Splitting with Co-doped-hercynite

Testing and Characterisation / Heat Integration

Tor Olav Høva Erevik

NTNU, 2016

Master Thesis

PREFACE

This master thesis has been written within the research group of Environmental Engineering and Reactor Technology within the Department of Chemical Engineering at NTNU.

First of all, I would like to thank my supervisors, Professor Magne Hillestad and Professor Erling Rytter, for their guidance and support throughout the project. I would also like to thank Nikolaous Tsakoumis for the assistance I got, even after leaving NTNU. Magnus Rotan and Kristin Høydalsvik Wells for the help I got with XRD.

CONTENT

ABSTRACT

By using concentrated solar energy, it is possible to split water to hydrogen and oxygen, or eventually CO_2 to CO and oxygen, by using redox materials at temperatures between 1200 – 1500 °C. One of the best redox materials studied so far, Co-doped-hercynite, has been synthesised by the incipient wetness impregnation (IWI) technique, characterised by surface area/pore measurements (BET/BJH) and X-ray diffraction (XRD), and tested by thermogravimetric analysis (TGA). Successfully tested and characterised material had theoretical production capacities of H_2 or CO per mass Fe similar to the ones of other Co-doped-hercynite produced earlier by more advanced techniques. Activity was confirmed for 12 subsequent isothermal redox cycles at 1400 °C. Results and considerations imply that the total yield per mass Fe is dependent on the concentration of Co.

Under certain conditions, oxidation was observed to start at about 500 °C, and reduction to start at as low as at around 1000 °C, which is the lowest reduction temperature recorded for Co-doped-hercynite. During CO_2 splitting cycles, weight change fluctuations seemed to occur during oxidation, which could be related to simultaneous reduction activity, and another observation indicated carbonization. Observations were also in accordance with theory regarding increasing formation rate of Co alumina compounds when calcination occurs under inert atmosphere. A kinetic study to determine the reduction reaction model was also performed, where the D3 and D4 model seemed to be the best fits.

Results from X-ray diffraction strongly indicated formation of α-alumina for all samples made and calcined at only 1000 °C overnight. Apart from this, the expected phases were identified for all samples at the different calcination temperatures, and the XRD pattern of cycled material was found to be as good as identical to a previously reported cycled Co-doped-hercynite material. BET showed an increasing surface area and pore volume the higher metal loadings, but this have to be confirmed by further studies. Samples prepared by calcination at 300 °C is believed to be at least about 200 m^3/g, and at least about 8 m^3/g when calcined at 1000 °C in air.

In addition to experiments, evaluation, testing and further development of the method used for heat integration of a particularly cost efficient process design, studied in the specialisation project prior to this master thesis, was performed. An efficient heat integration is particularly crucial for the profitability of solar thermal splitting processes. The primary cost driver for the process is likely to be the cost of heliostats, and in this supplementary work, an automated techno-economic procedure to balance heat recovery against the cost of heliostats was accounted for.

*

INTRODUCTION

The sun is important source of renewable energy, and ways of storing and harvesting solar energy efficiently are in rapid development. Solar energy can be exploited actively through the use of either photovoltaic systems, concentrated solar power or solar water heating. Photovoltaic systems are systems designed to produce electricity by converting sunlight into electricity by using solar panels. A concentrated solar power system uses mirrors or lenses, called heliostats, to focus a large area of sunlight into a small area in order to either drive a heat engine to generate electricity or power a thermochemical reaction. Powering thermochemical reactions through heliostats are still at the exploratory level. This master thesis treats a case where heliostats are used to power such a process; thermal splitting of water to hydrogen and oxygen, and eventually CO_2 to CO and oxygen to produce fuel. Such a process has several potential advantages over the other methods of storing solar energy. Firstly, the product is ordinary fuel, and does not require new, revolutionary methods of storing energy. Transporting thermal heat over long distances, for instance, is much more difficult than for ordinary fuel, and electricity production would often require long power lines transporting electrical energy. Secondly, high theoretical energy efficiencies are possible, because energy from the entire solar spectrum is used directly to drive the redox reactions [1]. By contrast, most commercially available solar cells have an energy efficiency of typically 10 – 20 % [2, 3]. Moreover, the type of thermochemical process studied here is chemically simple, and requires less land and water than competing biomass plantations, artificial photosynthesis and photovoltaic-driven electrolysis [4].

*

In the main part of this master thesis, one of the best redox materials studied so far, Co-doped-hercynite, that can be used to split water and alternatively CO_2, have been synthesised, characterised and tested, and a kinetic study has been done. The incipient wetness impregnation (IWI) technique has been used to synthesize the material. So far, these oxides have mostly been prepared through atomic layer deposition (ALD), which is typically a more expensive fabrication technique [5]. The second part of this thesis will deal with evaluation and further development of the method used for heat integration of a particularly cost efficient process design, studied in the specialisation project prior to this master thesis. An efficient heat integration is particularly crucial for the profitability of solar thermal splitting processes. To get an overview over the overall process and to demonstrate how the solar thermal splitting process can be utilized, the general concept and particular design to be optimised are presented first. Subsequently, improvements to the method will be discussed before introducing the experimental part.

1 PROCESS DESCRIPTION

1.1 General concept

The particular choice of concentrated solar power system that was optimized with respect to heat integration in the previous specialisation project is based on previous studies at NTNU [6], comparing different configurations. In general, synthesis gas, or syngas, which is CO and hydrogen, is being produced from water and CO_2, which can be done by using metal oxide redox materials at high temperatures between 1200 and 1500 °C [1]. It is of course also possible to only produce hydrogen or CO. The high temperatures are reached by using concentrated solar energy. The reaction has an oxidation step and a reduction step. In the oxidation step, the metal will pick up an oxygen atom from water or alternatively CO_2, thus yielding either H_2 or CO. The product is then removed for further processing. When the partial pressure of steam is being reduced, the oxidised metal will eject the oxygen atoms, thus being reduced again, and oxygen gas is produced. A simplified sketch of an oxidation-reduction cycle for water splitting is given in Figure 1.1.

The oxygen gas has to be removed before the next cycle, especially if hydrogen is present, or else hydrogen product will react with oxygen back to water once more. The oxygen can be removed by using an inert gas or vacuum. Thus, by splitting water or CO_2 in two steps, one will avoid recombination back to reactants. If the thermochemical splitting would occur in one, single step, which is called direct thermolysis, one would need to separate the products at

*

extreme temperatures, which would be very difficult to achieve [1]. Besides, single-step

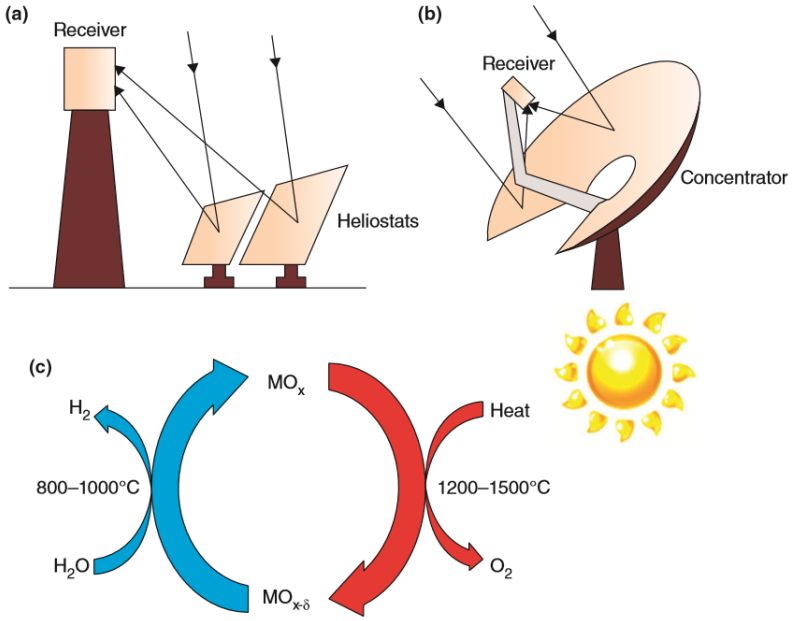

Figure 1.1: c) Oxidation-reduction cycle for water splitting. MO_x denotes oxidized metal, while $MO_{x-\delta}$ denotes reduced metal. a) How solar power is concentrated through heliostats and a power tower. b) Alternative solar power collection by a parabolic dish concentrator [1].

splitting of water requires a temperature above 2200 °C for even minimal reaction extents, which makes it impractical [1]. Optionally, the cycles could involve more than two steps, which is called multistep cycles. These cycles do often involve the use of a metal in combination with strong acids or bases, together with an electrolysis step. Although many of these cycles operate at a maximum temperature below 900 °C, they are believed to be less profitable that simple two-step cycles to produce hydrogen. The reason for this is that multistep cycles would involve the use of dangerous chemicals, design complications and energy inefficiency related to the numerous process steps [1].

In any case, hydrogen will be produced through what is called "Solar Thermal Water Splitting." This hydrogen could either be sold directly, or be mixed with CO to yield syngas. The pure oxygen formed is also to be considered as a valuable product. Optionally, CO_2 can be split in the same way to form CO. Another alternative is to let CO_2 react with hydrogen at elevated temperatures to form CO and water. This is what is called the "Reverse Water Gas Shift" (RWGS) reaction. An advantage by choosing this instead of thermal splitting of CO_2 is avoiding the risk of coke formation in the solar reactor. The amount of CO_2 feed can be

adjusted to produce the optimal molar ratio of hydrogen to CO (H_2/CO ratio) in the synthesis gas. The optimal ratio will depend on which process the synthesis gas is intended for. Relevant use of synthetic syngas could be methanol production or synthetic fuel production through the Fischer-Tropsch (FT) process.

1.2 Configuration to be optimized

The process that needs to be optimised with respect to heat integration is a process where syngas is produced for production of liquid fuel (gas-to-liquid; GTL) through the Fischer-Tropsch (FT) process. The optimal H_2/CO ratio for a FT process where cobalt-based redox materials are used, will be around 2, and was used as target basis [7]. Previous studies had indicated the isothermal, or near-isothermal, "doped-hercynite cycle" to be a promising one for water splitting, and was therefore integrated in the simulations.

The heat integration simulations will be carried out on a particularly promising process design for syngas production, studied recently at NTNU. In a study performed by Lundgren et. al., different process configurations for a syngas production with a H_2/CO ratio of 2 were compared. Two different configurations were indicated as most profitable, and a block diagram of the process configuration to be studied is given on Figure 1.2 below.

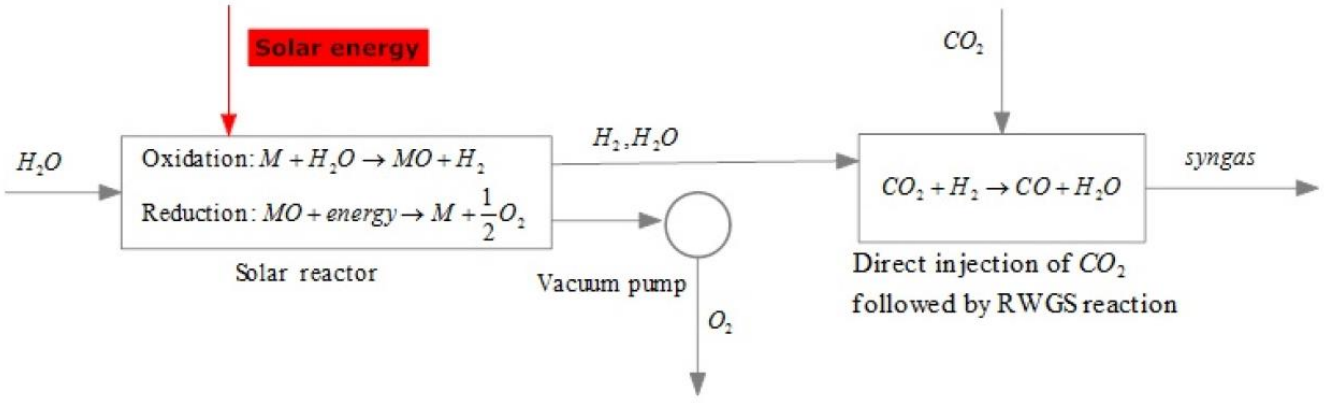

Figure 1.2: The block diagram of the process to be studied. First, water is converted to hydrogen and oxygen in the solar reactor. The hydrogen and unconverted water is mixed with CO_2 to shift some of the CO_2 over to CO by the RWGS reaction to yield syngas. When the

*

partial pressure of oxygen is reduced by a vacuum pump, the oxidized metal will release oxygen that is flushed out separately. Some of the unconverted water is likely to be flushed out with the oxygen.

In this design, which is referred to as Configuration 1B in the report by Rytter et. al., oxygen is flushed out of the reactor by the use of a vacuum pump operating at 0.5 bar, and hydrogen produced by water splitting reacts with CO_2 through the RWGS reaction to produce the syngas. The other most promising option was Configuration 2B, where oxygen still is flushed out at 0.5 bar, but with both water splitting and splitting of CO_2 in two separate reactors to yield CO and H_2 directly without any RWGS reaction.

Rytter et. al. concluded that Configuration 1B needed to be further optimized to give grounds for a better comparison between the two options. This could be done by optimizing heat integration while doing a pinch analysis. In the previous study, no pinch analysis was done when comparing the different configurations. Previous studies have shown that the primary cost driver for various solar thermochemical hydrogen production processes is the cost of heliostats [9-11]. Thus, an efficient heat integration to elevate the temperature of the steam feed to the solar reactor as high as possible is critical to economic feasibility. The base case steam inlet temperature to the reactor in Configuration 1B was initially set to only 317 °C. If the inlet temperature is increased, the investment cost could be significantly reduced by lowering the need for expensive heliostats. However, preheating CO_2 is needed to secure a high enough temperature to be close to equilibrium without the need of catalyst and shift the equilibrium towards CO. Thus, increasing the temperature of the inlet steam comes at a price – there would be less heat available to preheat the CO_2.

In the previous immersive project, certain changes were made to Configuration 1B. For specific details about these, as well as general assumptions and product specifications, please refer to the specialisation project report. However, since the focus here is the heat integration methodology, the description already given should be adequate. Certain process specifications set in the prior project should have been different, and these are discussed in Section 1.5.

1.3 Main challenges and aspects of the heat integration

The operation temperature in the solar reactor is 1350 °C, and the oxygen product stream needs to be cooled down from this temperature. At such high temperatures, conventional heat exchangers are not suitable. The annealing temperature of nickel for instance, is 1150 °C, while it is 1050 °C for stainless steel (18Cr, 8Ni) [12](p. 399). It is therefore reasonable to assume that exotic materials are required above 1100 °C for a gas-to-gas heat exchanger. Optionally, a waste heat boiler (WHB), could be used to cool the oxygen stream from 1350 °C to 1100 °C. The principle of a WHB is sketched in Figure 1.3 below.

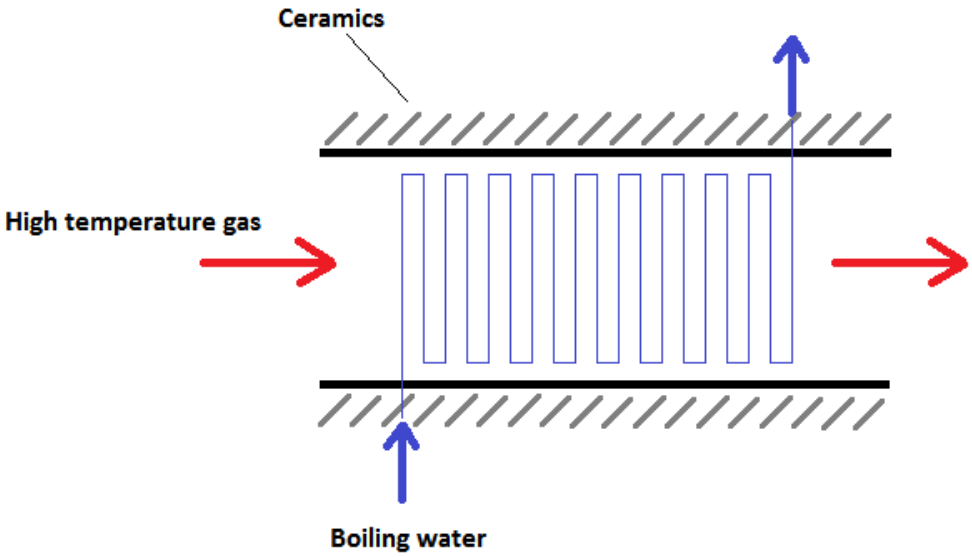

Figure 1.3: The principle of a waste heat boiler (WHB). High temperature gas is flowing between coils of boiling water. When boiling water is flowing inside the coils, the outside temperature of the tubes will be considerably lower than in the bulk phase, thus protecting the tubes against thermal deformation. The outer wall of the WHB is typically made of thermally stable ceramics.

When water is boiling inside the tubes in the WHB, the outside temperature of the tubes will be considerably lower than in the bulk phase, thus protecting the tubes against thermal deformation. In addition, at high concentrations of oxygen in the hot stream, a protective oxide layer is likely to be formed on the outer tube wall. A WHB is typically not much more expensive than regular heat exchangers. On the other hand, according to a customer representative at Heat Transfer International (HTI), a company that is producing high temperature ceramic heat exchangers for temperatures up to 1315 °C, a gas-to-gas high

*

temperature heat exchanger would cost from 10 to 20 times more than a conventional heat exchanger. He advised using a factor of 20 to be conservative in early estimates. The high cost is due to the need of expensive, exotic materials. Furthermore, dirty gas has to be cleaned before entering HTI's high temperature heat exchanger. This will not be a problem in this case, though, since all stream compositions are assumed to be non-corrosive, without any traces of sulphur or similar. Fortunately, there is no size limitation to these heat exchangers – they are easily scalable. It is also possible to create hybrid heat exchangers, using less expensive materials near the outlet of the hot stream where the temperature is low enough. Figures of some possible designs of HTI's ceramic high temperature heat exchangers are shown on Figure 1.4 below [13, 14].

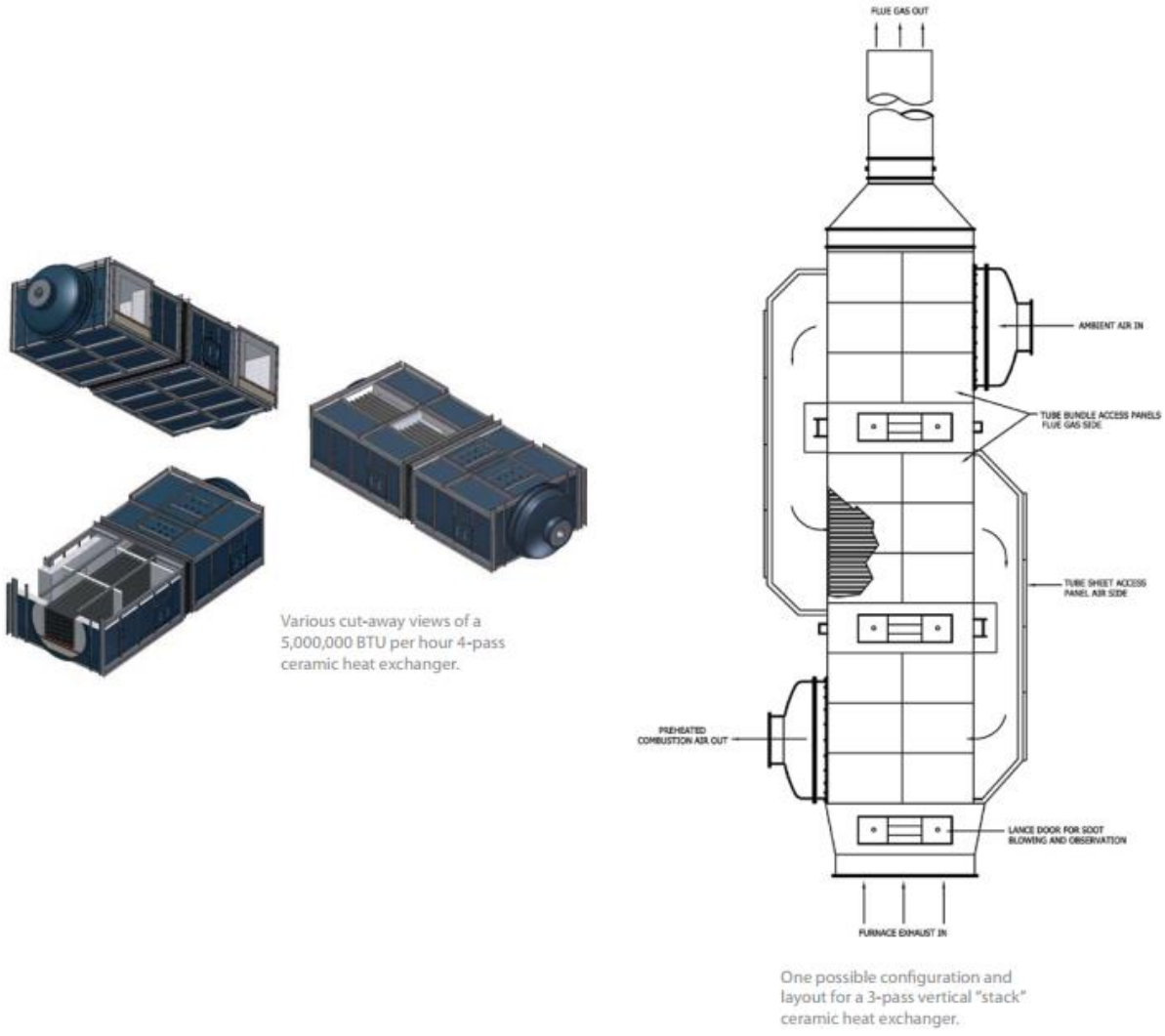

Figure 1.4: Sketches of the design of Heat Transfer International's high temperature ceramic heat exchanger.

The downside of using a WHB instead of a high temperature heat exchanger (HTHE) is that a WHB can only be used to produce steam. With a HTHE, the high temperature heat could be used to superheat steam entering the solar thermochemical reactor in the upper temperature interval for instance, so that the need for expensive heliostats would decrease. The lower temperature of the steam entering the reactor, the lower duty needs to be delivered from the heliostats. It could also be possible that using a HTHE on the hydrogen product stream to superheat the steam to a certain extent instead of mixing it directly with CO_2 could pay off for the same reason.

The use of at least two WHBs is nonetheless inevitable; one on the reactive and corrosive hot syngas product stream, and the other one at the corrosive tail gas out from the auto thermal reformer (ATR) in the FT process section. It is assumed that WHBs are needed until the temperature of both streams have been cooled down to 600 °C. In addition to prevent corrosion, the hot syngas product should be cooled down to below around 850 °C as quickly as possible, because the RWGS reaction will happen spontaneously at temperatures above about 875 °C [13]. If cooled down too slowly, time would allow the equilibrium to shift over to CO_2 and water to a greater extent as the temperature decreases, which is undesirable. Letting the hot syngas cool down through a WHB is a good way of reducing the temperature quickly, since heat transfer happens most efficiently between boiling fluids.

Previous solar-to-hydrogen efficiency studies performed by Muhich et al. and Ermanoski et. al. have also emphasized gas-to-gas heat recovery as a decisive factor for the overall efficiency [1, 15]. It is especially critical for isothermal water splitting (ITWS). A gas-to-gas heat recuperation of 100 % at isothermal reactor conditions would lead to the highest possible efficiency [1]. Ermanoski et.al. state that high levels of gas-to-gas heat recovery, more than 97%, are possible up to about 650 °C using heat exchangers of stainless steel. This efficiency could also be reached using printed circuits heat exchangers, which can operate at temperatures up to 1000 °C [16]. Furthermore, both groups claim that heat exchangers of nickel alloys could be deployed up to about 1000 °C. Muchic et. al. also contacted some producers of ceramic heat exchangers, and were informed that heating gases up to 1200 °C is

*

almost guaranteed, 1300 °C should be achievable, and 1500 °C should be possible, maybe even higher. They too, recognize the need for an economic analysis to determine if ceramic heat exchangers should be used.

1.4 Description of method used for heat integration

Different alternative configurations of heat exchangers have been compared using Aspen Energy Analyzer, which can determine the size and cost of distillation columns and heat exchangers. The program is able to optimize heat exchanger networks (HENs) automatically through the Automatic Recommended Design (ARD) feature. The optimization is done with respect to the following parameters [17]:

- "Process and utility stream supply and target temperatures."
- "Process stream's heat loads."
- "Temperature-dependent specific heat and heat transfer coefficients for each stream."
- "Operating cost per unit heat load of each utility."
- "Capital cost of placing a heat exchanger on each possible match."

To compare different HEN configurations, simplified HYSYS files of the relevant configurations were imported into Aspen Energy Analyzer. For each of the configurations, 50 different optimised HEN designs were generated. The one of the 50 with the lowest total annual cost and no infeasible HEs was chosen for comparison. The methods used by the program for size and cost calculations are developed for the preliminary configuration analysis, where the focus is on the relative comparison of various design options, and not the absolute costs. For more detailed cost analyses, the HYSYS Economix software package can be used [17]. In the previous project, however, only a relative comparison between different HEN configurations has been done, and Aspen EA would thus be sufficiently accurate.

For preliminary configuration analysis, the program is still able to take many factors into account to give a reasonable sizing and cost estimates. To calculate the fixed cost of heat exchangers for instance, design pressure, type of heat exchanger and installation costs are determined by various formulas with many different coefficients, where the coefficients can be manipulated manually. The default specifications and limitations for fixed costs are stated below, retrieved from the user reference guide [17]:

- "The equations are valid for heat transfer area between 14 m^2-1 100 m^2."
- "The program provides default coefficient values for three different sets of pressure ranges. The program will automatically select the appropriate coefficient values based on the heat exchanger operating pressure."
- "The program provides default coefficient values for a fixed head heat exchanger."
- "The program provides the default coefficient values for the construction material of carbon steel and the assumed operating pressure at 700 kN/m^2."
- "The equation used for calculating installation costs is valid for a heat exchanger purchase cost between $9,500-$240,000 US dollars."

Here one can see two apparently contradictory statements; the appropriate coefficient values are selected automatically from three different sets based on the operating pressure, while the operating pressure is assumed to be 700 kN/m^2, 7 bar, at the same time. The meaning of this was found unclear.

The operating costs are time dependent costs or revenues related to the operation of utility streams, i.e. external energy sources like cooling water, steam generation or fired heaters. The operating cost for steam generation will be negative, which would mean that revenue is generated by selling the steam. The operating cost is included in the total annual cost, which also takes into account the following factors [17]:

- "Interest rate. This is the time value of money."
- "Plant life. This is the operational life of the plant or time period for which the plant operates."
- "Inflation. This is the change of equipment value over time."
- "Total cost of the column. This includes the purchase and installation costs."

*

A screen shot of the user interface for economics in the program is found on Figure 1.5.

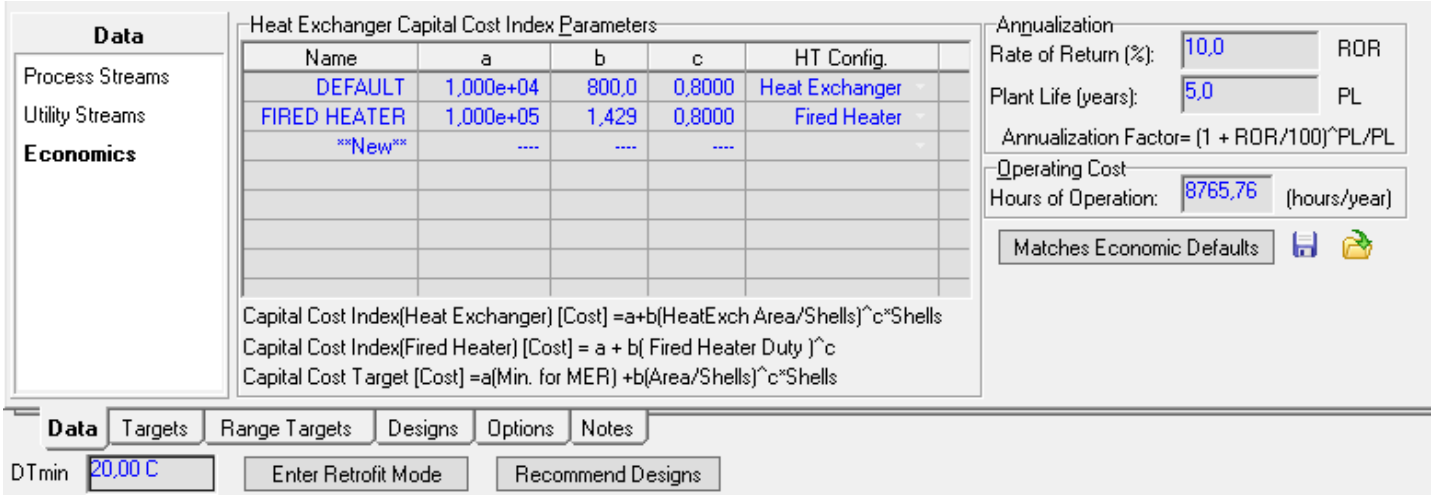

Figure 1.5: The user interface for economics in Aspen EA. All values in the tables are default ones, except DTmin, the minimum temperature difference between cold and hot process streams, which has been set to 20 °C instead of 10 °C.

According to the user reference guide, more cost parameters than the ones given in Figure 1.5 can be manipulated manually. In this work, however, only the cost and annualization parameters seen in Figure 1.5 were changed.

1.5 New premises, corrections and suggested method for heat integration

In the specialisation project, Configuration 1B was investigated and optimized fairly, and a method for optimizing the heat integration was developed. The heat integration could, however, have been done more efficiently. Firstly, more of the process could be imported into Aspen EA to ease calculations, as well as optimising more of the process. If heliostats are included as a hot utility stream with correct cost parameters, the inlet temperature to the reactor could be optimized automatically through a techno-economic optimisation, which in fact is the final goal. However, as mentioned in Section XX, the program was not originally developed for a detailed costs analysis. Still, a relatively good economic optimisation is believed to be possible, as long as costs of different heat exchangers and utility streams are realistic. The new method proposed is discussed in Section XX-YY below.

1.5.1 New important simulations premises

- Since the hot syngas produced is both reactive and corrosive, it should be assumed that it is required to use a WHB to cool this stream down to at least 600 °C. The tail gas stream from the auto thermal reformer (ATR) in the FT section is also highly corrosive, so the same requirement should be set here.
- The pressure of the oxygen stream out from the reactor should be set to 0.1 bar instead of 0.5 bar. This is believed to be more realistic.

1.5.2 Updated equipment costs

The year of basis for the cost parameters used by default in the program is unknown. Thus, new parameters should be determined by using the factorial method explained by for instance Towler and Sinnot, and a base year should be chosen. In January 2016, a company announced that the price for their concentrate solar plant heliostats would be likely to cost 100 €/m^2 [18, 19], and this point in time could be an example of a good basis. The percent of direct normal insolation (DNI) from the sun down on the heliostats that eventually becomes available for heating of water or driving the reaction, η_{coll}, is estimated to be 35 % [20]. The max cumulative DNI in South Africa is 3200 kWh/yr·m^2 [21], and by dividing by hours of operation per year, which has previously been counted as hours of sunshine per year, one obtains the DNI. Hours of sun per day is about 8.5 in South Africa [22]. When multiplying DNI with η_{coll}, one gets the duty available per area of heliostats. This number can be divided by the investment cost per area, which will give an energy cost of $8.34 \cdot 10^{-2}$ 2016-USD/(kJ/h). This value can be set as *b* for a new fired heater cost set, as seen in Figure XX, while *a* equal to zero and *c* equal to 1. The operation costs can be estimated to be about $6.64 \cdot 10^{-6}$ 2010-USD/kJ [23].

Next, the “Forbidden matches” tool can be used to prohibit matches with other streams than steam going into the solar reactor. However, prohibitions made here are often ignored, so it is better to specify a new cost parameter set of very high *a* and *b* values, and specify this set to

*

count for the forbidden matches. However, heat loss when pressure is relieved, the extra cost of heating to account for the heat loss has to be added to the total annual cost.

1.5.3 WHBs and high temperature heat exchangers

Both WHBs and high temperature heat exchangers can be included in Aspen EA as optional alternatives for the program to choose from. The cost of using high temperature heat exchangers could be set to 20 times that of regular ones, as explained in Section XX. This is done by adding a cost parameter in Figure XX where *a* and *b* is set to be 20 times higher than for an ordinary heat exchanger. The WHBs can be simulated as steam generating cold utility streams. However, steam generating utility streams can only be used to model the boiling part, not heating of feed water. It was tried to segment these streams manually into a water heating part and a boiling part, but this only resulted in a non-boiling outlet temperature, since the outlet temperature of utility streams are free variables. Nonetheless, this problem could be evaded by scaling the operational revenue of selling the steam down to the true value. A certain amount of heat from a stream Q_1 at a too high steam production rate would still be equal to the heat Q_2 needed to be remove the heat from the same stream given a lower steam production rate due to initial heating of water. Q_1 and Q_2 could be expressed as followed:

$$\boldsymbol{Q_1 = \dot{m}_1 \Delta_{vap} h} \qquad (1.1)$$

$$\boldsymbol{Q_2 = \dot{m}_2 (c_p \Delta T + \Delta_{vap} h)}$$

Where $\boldsymbol{\dot{m}_1}$ is the too big flow of steam, while $\boldsymbol{\dot{m}_2}$ is the actual one, $\boldsymbol{c_p}$ is the average heat capacity of the heated water, and $\boldsymbol{\Delta T}$ is the temperature difference between feed water and boiling water. Since Q_1=Q_2, it can be shown that:

$$\boldsymbol{\dot{m}_2 = \dot{m}_1 \cdot \frac{\Delta_{vap} h}{c_p \Delta T + \Delta_{vap} h}} \qquad (1.2)$$

Since the amount of steam sold would be proportional to revenue, the actual revenue of selling the steam could be scaled down in the same manner. Given a certain general profit

from selling steam, which is given in terms of USD/kJ steam in Aspen EA, one could multiply this number with the same factor as seen to the right in Equation (1.2). The capital cost of the WHB could be scaled in a similar manner.

Steam is often allowed to condensate and evaporate in recirculation loops within the heat exchanger network, which results in high overall heat transfer coefficients. To open up for this, corresponding hot steam utility streams could be added too. In this process there are, however, much excess heat at lower temperatures at around 200 °C, so there will be a net steam generation.

1.5.4 FT reactor coils

The FT reactor coils are a type of exchanger that could be integrated in Aspen EA as well. If assuming Utot=1500 W/m2C when boiling and Utot=1000 when not boiling in the reactor for instance, one could calculate the outside fluid film coefficient. The coils could be assumed to be cylindrical tubes, for instance, and the cost per area could be found and inserted as *b* in the economics tab.

1.5.5 Fluid film coefficient

The fluid film coefficient, called the heat transfer coefficient (HTC), for boiling streams could be raised to higher values if they are found to be small compared to other high pressure liquid streams for instance, to reflect that heat exchanging with boiling liquids always are most efficient. During testing, this was experienced, and consequently, the default values set for water boiling were raised. The exact values set are believed to be of little significance, since the overall heat transfer coefficient would be almost independent of the boiling fluid film coefficient because of the high values.

1.5.6 Plant life and hours of operation

The default economic parameters plant life and hours of operation per year could be changed from default values to more realistic ones. Plant life could have been changed from default 5 years to 20. Hours of operation per year is 8765.76 by default, which means continuous

*

operation throughout the year. Since direct solar energy is needed to run the plant, it is assumed that hours of operation per day will be equal to the hours of sunshine per day where the plant is located. In South Africa, which was considered to be the most optimal location for the solar plant by Lundgren et. al., the average hours of sunshine per day is 8.5. Multiplied by the number of days per year, one will have 3104.56 operational hour per year.

1.5.7 Wrong inbuilt method for calculating total annual cost has been compensated for

According to the Aspen EA reference guide [17], the total annual cost (TAC or C_a), which is minimized during optimization, is calculated by the following equation:

$$\boldsymbol{TAC = \Lambda \cdot \sum CC + OC} \qquad (1.1)$$

CC is the installed capital cost of the heat exchangers, OC is the operating cost and Λ is the annualization factor. The annualization factor is given as follows:

$$\boldsymbol{\Lambda = \frac{\left(1 + \frac{ROR}{100}\right)^{PL}}{PL}} \qquad (1.2)$$

ROR is the rate of return, while PL denotes the plant life. However, this annualization factor does not correspond to the factor that is normally used, which is called the annual capital charge ratio (ACCR). The ACCR is defined as follows []:

$$\boldsymbol{ACCR = \frac{i(1+i)^n}{(1+i)^n - 1}} \qquad (1.3)$$

i is the interest rate, while *n* is the number of years. It is common to add cost factors to the ACCR for a complete plant, but here only the HEN is considered. When *PL* is increased, *Λ* will also increase. That means that a big initial investment to provide an efficient heat integration by minimising the use of utility streams is more profitable for a short plant life than a long plant life. This is not logical; it should be opposite. Another expression for the annualization factor, denoted as F_{an}, is actually given in the last page of the reference guide, which is identical to the one in Equation (1.3). Here, the TAC is given as:

$$\boldsymbol{TAC = F_{an} \cdot C_{CC} + (1 - F_{it}) \cdot \text{operating cost}} \qquad \textbf{(1.4)}$$

C_{cc} is the total capital cost of the columns and heat exchangers, and F_{it} is the income tax factor. However, it is assumed that Equation (1.3) and (1.4) is used for calculating the cost of distillation columns and appurtenant heat exchangers, although it is not clearly expressed. It is also stated that the annualization factor is equal to the one in Equation (1.2) in the "Economics" tab user interface in Aspen EA. To check whether Equation (2.1) or (1.4) is used for HEN optimization, the TAC for the optimized HEN of Configuration 1 from the previous report, but where plant life was set to 200 years instead of default 5, was calculated manually by both equations. The variables needed to calculate the TAC is total capital cost, operating cost, hours of operation per year and F_{it}. The first two is calculated automatically by Aspen EA, while hours of operation per year is 8765.76 by default, which means continuous operation throughout the year. The TAC given in Aspen EA was unrealistically high, 57 226 USD/s, and deviated from the one found manually by Equation (2.2) with less than 0.01 %. The TAC found manually by Equation (1.4) gave much more realistic values, lying between 0.60 and 3.45 US¢/s when varying F_{it} between 1 and 0. Thus, it can be concluded that Equation (2.4) is used when optimizing the HEN.

Aspen EA has been made to use the ACCR by calculating the factor manually. Then, ROR has been set to zero in the program. Next, if Equation (1.2) is to be equal to the value found by Equation (1.3), then PL has to be set equal to the inverse of this value:

$$\boldsymbol{\Lambda = \frac{\left(1 + \frac{0}{100}\right)^{PL}}{PL} \overset{!}{=} ACCR}$$
$$\boldsymbol{\rightarrow PL = ACCR^{-1}} \qquad \textbf{(1.5)}$$

*

2 LITERATURE REVIEW

2.1 Basis for investigation – Why hercynite?

Substantial research has been done to find efficient and robust redox materials for driving STWS in as practical conditions and high reaction rates as possible. The ideal STWS material has [1]:

- "High H_2 production capacity
- Low reduction temperature
- Fast kinetics
- Long lifetime
- Compatibility with containment materials
- Nontoxic composition
- Low cost"

The first three factors are the major characteristics that determine the overall efficiency of the system, while the others affect the cost and potential dangers of operation [ny artikkel]. The higher operation temperatures, the more heating duty is needed from expensive heliostats, and the reduction step is always requiring a higher temperature than oxidation, and is typically the rate determining one [1]. A low reduction temperature also means that one would be more capable of operating isothermally, which would be favourable for the overall efficiency of the

process one [1], which is explained in Section 2.2. One can categorize two-step water splitting cycles into three groups by their reaction mechanisms:

- Volatile stoichiometric chemistries
- Non-volatile stoichiometric chemistries
- Oxygen vacancy chemistries

Both the volatile and non-volatile chemistries involve generation of a stoichiometric quantity of oxygen, 0.5 moles, and hydrogen, 1 mole, for each mole of reacting oxide as the material is being reduced or oxidized, respectively. Until 2015, the Co-doped-hercenyte cycle, which was discovered in 2010 by Scheffe et al. [1] was believed to follow the subsequent non-volatile stoichiometric mechanism [8, 10]:

$$\begin{aligned} CoAl_2O_4 + 2FeAl_2O_4 + H_2O &\rightarrow CoFe_2O_4 + 3Al_2O_3 + H_2 \\ CoFe_2O_4 + 3Al_2O_3 + heat &\rightarrow CoAl_2O_4 + 2FeAl_2O_4 + \frac{1}{2}O_2 \end{aligned} \tag{0.1}$$

As one can see from the reaction equations, solid metal alumina spinel compounds are oxidized to metal spinel and alumina, which are transformed back to metal alumina again during reduction. Since none of the products are gaseous, as in the ZnO cycle for instance, where the reduction step is ZnO → Zn *(g)* + ½ O_2, it is non-volatile [1]. However, in 2015 it was shown by Muhich et al. that the Co-doped-hercynite cycle rather operates through an oxygen vacancy mechanism [1, 24, 25]:

$$\begin{aligned} Co_{0.5}Fe_{0.5}Al_2O_{4-\delta_{red}} + \Delta\delta H_2O &\rightarrow Co_{0.5}Fe_{0.5}Al_2O_{4-\delta_{ox}} + \Delta\delta H_2 \\ Co_{0.5}Fe_{0.5}Al_2O_{4-\delta_{ox}} + heat &\rightarrow Co_{0.5}Fe_{0.5}Al_2O_{4-\delta_{red}} + \frac{\Delta\delta}{2}O_2 \\ \Delta\delta &= \delta_{red} - \delta_{ox} \end{aligned} \tag{0.2}$$

In an oxygen vacancy mechanism, oxygen is realised by the formation of oxygen vacancies in the active metal oxide lattice, and involves no other changes in the crystal structure. If the materials are allowed to fully oxidize, δ_{ox} is zero. This is often a reasonable assumption, since oxidation happens much faster than reduction [8, 26]. If δ_{ox} is zero, the equation becomes [25]:

$$\begin{aligned} Co_{0.5}Fe_{0.5}Al_2O_{4-\delta} + \delta H_2O &\rightarrow Co_{0.5}Fe_{0.5}Al_2O_4 + \delta H_2 \\ Co_{0.5}Fe_{0.5}Al_2O_4 + heat &\rightarrow Co_{0.5}Fe_{0.5}Al_2O_{4-\delta} + \frac{\delta}{2}O_2 \end{aligned} \tag{0.3}$$

*

Here δ denotes δ_{red}. δ is dependent of temperature, pressure and type of material [15, 20]. Most of the early research was focused on stoichiometric mechanisms, but recently this has shifted over to O-vacancy based ones [1]. Stoichiometric cycles have high hydrogen production capacities, but most of the ones studied so far are inclined to form gas or liquid phases upon reduction, which make it hard to implement these materials in practice. The operation temperatures typically need to be close to the melting temperature of the metal compounds. Thus, efficient techniques to prevent sintering has yet to be developed before one could deploy these materials [1]. In practice, such materials suffer from deactivation caused by irreversible processes such as sintering, erosion, deactivating liquid phases or other undesirable phases and metal vaporization, which lead to loss of active oxide [4, 27]. In hercynite cycles, however, the metal alumina compounds formed are believed to be stable at the necessary operating temperatures between 1200 and 1500 °C [1, 28].

Stability and consistent hydrogen production capacity have been confirmed experimentally for more than 200 subsequent cycles by Weimer et. al. at reduction carried out at 1500 °C, and oxidation at 1350 °C [26]. In these cycles, the hydrogen production capacity of the material was tested by heating and cooling the samples back and forth between 1350 and 1500 °C, with 50 mol% steam in inert helium at oxidation, while flushing only helium at reduction [25]. This operation mode is an example of a mix between temperature swing cycles and pressure swing cycles, where oxidation and reduction of the material is controlled by temperature as well as the partial pressure of gases. An explanation and comparison between the two types of cycles is given in Section 2.2.

Although the doped-hercynite materials tested so far have relatively low reduction temperatures and high hydrogen production capacity, they are currently limited by slow reaction rates [1]. The other most studied O-vacancy-type materials are ceria-based ones, but these materials still require very high reduction temperatures in spite of years of research and doping with many different elements [1]. Perovskites, however, is another O-vacancy-type material, which produce significant amounts of hydrogen at relatively high rates with low reduction temperatures, and is mainly unexplored for use in STWS. Therefore, it is believed that continued research of known STWS cycles will focus on perovskites and doped-hercynite materials [1].

When Muhich et al. concluded that the Co-doped-hercynite cycle, as well as other aluminate redox spinel materials incidentally, operates through an O-vacancy mechanism in 2015, they developed a computational screening method to evaluate and identify candidate materials for STWS and their reaction mechanisms [24]. By using this method, they found that the hydrogen production capacity of Co-doped-hercynite should only be 70 % of that of un-doped hercynite, $FeAl_2O_4$, while the capacity for $CoAl_2O_4$ should only be 0.02 % of that of $FeAl_2O_4$. This means that un-doped-hercynite could potentially be a better STWS material than the Co-doped one. Nevertheless, the presence of Co will strongly increase the oxidation rate [24]. In this work, only Co-doped-hercynite has been investigated, but synthesized in a simpler way than earlier, which is explained in Section XX. Since Co-doped-hercynite has been more extensively tested previously, as seen in Table 4.1, it would be easier to evaluate the impact of fabrication method based on reported performance.

2.2 Temperature swing or pressure swing?

At low temperatures, oxidation becomes thermodynamically favourable, while reduction dominates at higher temperatures [1]. However, the temperature swings will submit the reactor and active materials to thermal stress, which can lead to thermal fatigue as previously experienced in temperature swing water splitting (TSWS) experiments [1].

In pressure swing cycles, the driving force behind oxidation is the high partial pressure of the oxidizing agent over the reduced product, p_{H20}/p_{H2} or p_{CO2}/p_{CO}, while the driving force for reduction is the low partial pressure of oxygen [1]. Thus, pressure swing cycles can be run at isothermal conditions, which can increase material lifetime as well as avoiding thermal and time losses related to the frequent heating and cooling, and lead to faster oxidation kinetics than in temperature swing schemes [1, 8]. Muhic et. al. showed experimentally that the hydrogen production capacity of isothermal water splitting (ITWS) at 1350 °C using Co-doped-hercynite can be more than 3 times greater per mass active material than TSWS of this material between reduction at 1350 °C and oxidation at 1000 °C, and more than 12 times for a then state-of-art ceria based material for the same TSWS cycles [8].

*

However, at elevated temperatures, reduction could happen simultaneously with oxidation, so that released oxygen from the active material could react with hydrogen product back to water once more, lowering conversion [25]. In addition, the low partial pressures of O_2 during reduction would either have to be achieved by energy demanding and technically challenging vacuum pumping, or large amounts of excess of inert gas sweep [1]. For this last reason, Ermanoski et. al. concluded that two-step isothermal cycles would be both impractical and inefficient, as when using vacuum pumping, inert gas or a mix of both, irrespective of reactor design or active material used [15]. An eventual inert gas sweep would lead to higher pump work and higher heat duties for steam heating, which would affect the overall efficiency and profitability of the system. When using inert gas, one would have to separate oxygen from the inert gas as well, which can be done by using membranes or by cryogenic separation. Because of the costs related to the use of inert gas, Rytter et. et. al found that using vacuum pumps would be more profitable when using concentrated solar energy to produce fuel through the FT process. This is why a vacuum pump is included in the design basis for heat integration, as seen in Section 2.2. Nevertheless, Lundgren et. al. compared only different designs options of isothermal cycles at 1350 °C. It is believed that a mix of TSWS and ITWS, near-isothermal water splitting (NITWS), would be the best solution, offering the highest theoretical efficiencies [1, 15, 26]. In this master thesis, however, Co-doped-hercynite has mainly been tested in isotherm pressure swing cycles at 1400 °C. The partial pressure of oxygen or CO_2 in the cycles has been controlled by using inert argon gas, while the total system pressure has remained unchanged. Details about the test method used is described in Section XX.

2.3 Synthetisation method

Up to this point, only atomic layer deposition (ALD), and a modified Pechini (citrate gel) method in 2015, have been used to synthesise Co-doped-hercynite [8, 24, 25]. ALD is a thin film coating technique that makes it possible to arrange the metal oxides is layers at desired ratios and thicknesses [29, 30]. ALD is done by using gaseous chemical precursors, which are compounds of desired material and functional molecules that reacts with the substrate, in this case alumina; Al_2O_3, until all of the substrate's surface is covered by one, single monolayer. Next, another set of precursors can cover the precursor already deposited, and by repeating this process over and over, one produces layer-by-layer of thin films of desired width [29]. For Co-doped-hercynite, the two precursors used have been cobaltocene and ferrocene [5, 31].

In general, the Pechini method is performed by using heat treatment on a mix of metal precursors, citric acid, water and a polyhydroxyalcohol to form a polymer matrix, which eventually is burnt off to form porous particles [32]. Muhich et. al. did not compare the performance of the materials designed by the two methods directly [24].

The reason why ALD was chosen as fabrication technique by Muhich et. al. was to ensure close contact between the metal and alumina support while simultaneously maintaining high porosity and surface area [5]. ALD has usually been seen as an expensive production technique, since valuable parts of the precursors are often lost during deposition. Muhich et. al. claim, however, that their procedure is very efficient because they use a fluidized bed configuration where nearly all of the precursors are being used [5]. At the same time, they state that ALD is not necessary to produce active materials. Depending on reactor design, desired mechanical material properties and similar, less expensive and simpler fabrication methods could be deployed to produce STWS active materials. As an example, Muhich et. al. mention spray drying of bulk Fe_2O_3, CoO and Al_2O_3 that initially has been blended or milled together in the desired stoichiometry. In this master project, a similar, simple method has been used, which is called the insipient wetness impregnation technique (IWI).

The IWI technique, also termed capillary impregnation or dry impregnation, is a method where one applies just as much solution with the desired solved precipitation material to the substrate support as required to completely wet the support. The amount of solution used corresponds to the total pore volume of the support [33]. When only this amount is being used, the driving force for absorption is capillary forces, which is much faster than ordinary diffusion which would dominate if excess solution would have been added. In wet impregnation, which is the other alternative impregnation technique besides IWI, excess solution is being used, but then a sufficient equilibration period allows a homogenous distribution of the precipitation particles, which could be metal precursors for instance, throughout the support [33]. When impregnation has been completed, the wet slurries are dried and calcined to remove water, eventual metal ligands and to reduce the metal to make it catalytically active. The distribution and sizes of precipitation particles in IWI depends on the mass transfer conditions within the pores during impregnation and drying [33]. When using this technique with salts, as being done in this work, one has to be careful that eventual salts

*

being dispersed are sufficiently soluble in the solvent, so that the liquid absorbed by the pores contains enough salts. Secondly, the solvent has to able to wet the surface of the substrate [34]. The Co-doped-hercynite was prepared by using Fe and Co salts completely dissolved in water, which is a solvent with high affinity for Al_2O_3.

3 METHODS AND PROCEDURES

3.1 Material composition

In this work, three samples of Co-doped-hercynite were made by IWI, one with about 10 wt% Fe and two with nearly 20 wt% Fe, all with a molar ratio of about 2:1 of Fe to Co. The actual wt% Fe for the samples were estimated to be not more than 9.56 wt%, 17.96 wt% for the first parallel and 17.94 wt% for the second one. Most of the Co-doped hercynite reported so far have similar compositions, as seen in table Table 4.1. The first parallel of the sample with about 20 wt% Fe is believed to have been more successfully synthesised than the second one, denoted by "20 % Fe (II)". The second parallel was not properly stirred as liquid was absorbed, and the ionic liquid added seemed to over-wet the alumina. It is suspected that more Fe and Co was absorbed in the first parallel. The first parallel was stirred continuously after adding the ionic liquid until it had cooled down and dried up. The other one was left without stirring overnight, and became very stiff as a result. It also seemed like the quartz holder in the calcination reactor was more blackened from the second parallel, indicating more ions sieving out from the sample. Nonetheless, the second parallel was tested and characterized anyways to illustrate the importance of proper synthetisation. Still, it might as well be that a deep penetration of Co and Fe in fact could have a negative effect on redox kinetics as well as process heating efficiency if this would lead to a lower surface metal concentration [35].

A detailed description of the synthetization procedure is found in Appendix 10.1.

*

3.2 Surface area and porosity – alumina support

A high surface area and porosity of the redox material is desirable because it would lower the diffusional resistance during reaction. For synthetisation, γ-alumina was used as support. This material is commonly used as support for catalysts because of its large surface area (>75 m^2/g [36]) porosity, acidity and low toxicity [37]. The more porous the starting material is, the greater pore volume, which means that more of the ionic liquid is able to penetrate the support during IWI. This will ultimately lead to a higher dispersion of active material [38]. However, when γ-alumina is heated, phase transition will begin at around 800 °C towards the much more crystalline α-alumina, commonly called corundum [36, 39, 40]. This leads to a big loss of surface area [38, 41]. On the other hand, the mechanical strength and sturdiness of α-alumina is very good [42], which is important when operating at high temperatures. Nevertheless, alternative methods for synthesising α-alumina with a greater surface area exist. Instead of direct high temperature calcination, one could calcine diaspore alumina at low temperatures, calcine gels or use a special hydrothermal technique [41]. None of these optional methods, however, have been used in this work. The effect of the high temperature calcination was studied by characterising synthesized material that had gone through only initial calcination at 300 °C, further calcination at 1000 °C in air overnight, and cycled material at 1400 °C respectively.

The extent of conversion to other types of alumina and crystal size depends on temperature and time of thermal treatment, as well as impurities and so called mineralizers. The presence of fluoride ions, for instance, can enable growth of corundum crystals at lower temperatures. Nevertheless, total conversion to α-alumina is known to occur when heating above 1500 °C for more than an hour [43].

3.3 Testing method

The samples made were tested by running oxidation-reduction cycles inside an apparatus (STA 449 C Jupiter, Netzsch-Gerätebau GmbH) performing thermogravimetric analysis (TGA) and differential scanning calorimetry (DSC) simultaneously. The apparatus was

connected to a gas distribution system. Since the system is partially open, the total pressure of the system is assumed to be equal to 1 atm. TGA is defined as measuring the weight change quantitatively as the sample is exposed to a temperature program. The weight resolution of the instrument used is 0.1 µg [44]. DSC is a technique where the difference in energy input into a sample and a reference material is measured, and is originally described by Watson et. al. The energy input difference corresponds to the heat flow associated with exothermic and endothermic transitions in the sample, or heating and cooling. In theory, integration of the area below the heat flow curve will yield the enthalpy change of the transition. However, to be able to quantify the heat flow correctly based on the measured temperature difference between the sample and the reference, one needs to calibrate the instrument by testing standard reference materials under same conditions and temperatures as the sample [44]. Furthermore, various effects, like static electricity or mechanical disturbances related to atmospheric changes for instance could affect the DSC signal [45]. The quality of the signal would also depend on the type and amount of sample, as well as crucible material and types of gases used [44]. In this work, no calibration has been done for DSC, but the measured signal could still be used to indicate chemical reactions qualitatively, supplementing the TGA measurements.

*

The TGA/DSC apparatus was also connected to a mass spectrometer (MS 403 Aëlos II, Netzsch-Gerätebau GmbH) as shown in below:

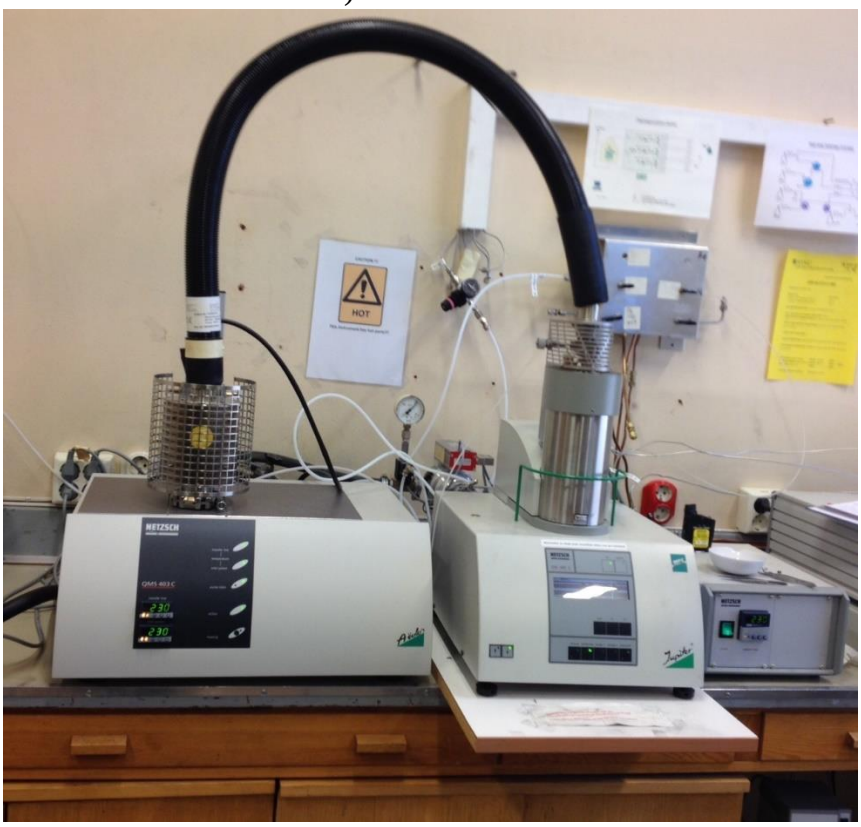

In general, mass spectrometry (MS) is analysis of matter through the formation of gas-phase ions that are detected and categorized by their mass and charge [46]. The mass spectrometer used can be calibrated to give quantitative analyses. Here, MS has only been used qualitatively to detect presence of certain molecular weights representing different compounds that could be present. It is not possible to tell from separately reported signals whether they are significant or not, but it can accompany the TGA measurements in the same manner as DSC. If abnormalities in the MS signal are detected, which are deviating from the trend, it could mean that something has gone wrong. If the detected signals for the molar mass of N_2 and N suddenly start to increase heavily in a point in the program where it has not done it before while only Ar is flowing through the system, then this would probably mean that there is a leak from the outside environment, since N_2 is the main constituent of air. Furthermore, the time needed to flush gases out of the system can be determined by looking at how the signal of the gas changes during flushing. The flushing time would be equal to the time before the signal stabilizes from the initial level to the final one.

3.4 TGA program specifications

Samples produced were tested in cycles alternating between oxidative and reductive atmospheres. However, a constant flow of protective Ar (25 ml/min) was required and always maintained. During reduction, only Ar (HiQ® Argon 5.0, AGA AS) was purged through the system. For oxidation, pure oxygen (HiQ® Oxygen 5.0, AGA AS), synthetic air (HiQ® Synthetic Air 5.0, AGA AS) and Ar, CO_2 (HiQ® Carbon dioxide 5.2, AGA AS) and 1 mol% O_2 in Ar (Spesialgass – 1% Oksygen i Argon, AGA AS) were tried respectively. Pure oxygen was only used initially during a non-isothermal program to give a clear indication on whether the produced material was active or not, and if so, at which temperatures oxidation is possible.

In isothermal cycle programs with oxygen, the oxygen level was tried to be held to a minimum, because high partial pressures of oxygen would oxidize the material very quickly. If oxidation happens too rapidly, it would be hard to visualize the oxidation lapse from the measurements. Consequently, the target concentration of O_2 was set to 1 V%. Since 50 V% steam has been used in most of previous reported water splitting cycles experiments, the same concentration was chosen for CO_2. Oxygen cycles were tried because testing with steam was not possible on NTNU, and it is assumed that performance of the materials produced using steam would lie in between the performance of using CO_2 and O_2 respectively. The reason for anticipating difference in performance is that it is generally harder to split CO_2 than water, because of stronger interatomic bonds in CO_2. Furthermore, custom-made gas with 1 mol% O_2 in Ar was tried instead of synthetic air in Ar, because of unexpected results when the latter was used, which is discussed in Section XX.

Each of the cycle programs had 6 continuous redox cycles, with 1 hour for reduction and 1 hour for oxidation, except for 45 minutes for the cycle program with synthetic air in Ar. In addition, a sweep with Ar was included after oxidation to remove oxygen or CO_2 as quickly as possible, as reported in earlier experiments […]. For the cycle program with synthetic air in Ar, a 1-minute sweep with Ar purge (150 ml/min) at a doubled flow rate of that used for the reduction step (75 ml/min) was used. In the sweep with Ar in the cycle program with CO_2, however, the Ar purge flow was only set to be 5 ml/min (30 ml/min) more than at reduction (25 ml/min). The reason for this was that it was decided to lower the flow rates from each of

*

the two purges of gases that could be used simultaneously to recommended rates specified in the operation manual for the instrument (20 – 30 ml/min). The protective flow of Ar comes from a third, separate purge, and was always maintained at 25 ml/min, as stated earlier. After analysing the MS signal change between oxidation and reduction step for CO_2, as seen in Appendix XX, the sweep time was decided to be increased to 2 minutes for the cycle programs where 1 mol% O_2 in Ar was used. More time was allowed to pass for the oxidation steps than what has been done in previously reported Co-doped-hercynite cycles, as seen in Table 4.1. It is not believed that this will increase the oxidation extent significantly, though, since oxidation happens much faster than reduction, which can be seen when looking at Figure XX-YY that is showing measured weight change with time. However, because of weight fluctuations at oxidation for many of the cycles, especially when using synthetic air and Ar, and CO_2, it was yet decided to let the oxidation run for 1 hour. The weight change from reduction to oxidation was then estimated as an approximate average of the weight measurements through the last 30 min of oxidation from the generally more stable end section of reduction. An overview of the program specifications can be found in Appendix 10.2.

All samples tested had been calcined at 300 °C in Ar before use, as described in Appendix XX, and were heated and reduced in Ar initially in the TGA program. However, starting with oxidative conditions and ending with reductive conditions was also tried with the 1 V% O_2 in Ar gas for the first parallel of the sample containing about 20 wt% Fe. Two such runs were made to yield enough reduced sample for characterization by X-ray diffraction (XRD). No mixed metal alumina compounds are assumed to be formed at only 300 °C, so it is assumed that the desired Co-doped-hercynite spinel phase will form during the first cycle. Starting in inert conditions is believed to speed up formation of metal alumina compounds, because the formation of CoO, which is reactive towards forming metal alumina, is more frequent under inert atmosphere [38]. Some of the samples were also calcined at 1000 °C in air in a calcination oven overnight for comparison with the other samples, inter alia to investigate whether Co-doped-hercynite could be formed at a temperature of 1000 °C.

The recommended amount of sample for each run for the instrument were 10 – 20 mg, which was only exceeded in the second run for yielding enough reduced sample for characterization by XRD (32.9 mg). For most of the other samples, the weight was near 20 mg.

3.5 Kinetic study

In this work, it was tried to determine the reaction diffusion model for reduction by analysing weight change with time for the first parallel sample of about 20 wt% Fe in the last reduction step in the Ar/1%O2 cycle program explained in Section X. As mentioned in Section XX and YY, reduction is the rate determining step, and the rate is assumed to be dependent of the rate of diffusion of oxygen out from the material. The rate of a solid-state reaction can generally be described by [47]:

$$\frac{d\alpha}{dt} = Ae^{-(E_a/RT)} f(\alpha)$$

Here, A is the preexponential (frequency), factor, E_a is the activation energy, R is the universal gas constant, T is the absolute temperature, $f(\alpha)$ is the reaction model, and α is the conversion fraction. For TGA, α is defined by:

$$\alpha = \frac{m_0 - m_t}{m_0 - m_\infty}$$

where m_t is the measured weight at time t, m_0 is the initial weight and minf is the final weight. Here, m_0 was set from the last point in the oxidation section, and m_inf was set from the last point in the reduction section. For the integral reaction model, $g(\alpha)$, at isothermal conditions one will have:

$$g(\alpha) = Ae^{-(E_a/RT)}t \qquad (0.4)$$

$g(\alpha)$ is defined as:

$$g(\alpha) = \int_0^\alpha \frac{d\alpha}{f(\alpha)}$$

A reaction model is a theoretical, mathematical description of what happens during an experiment, which is translated mathematically into a rate equation, as for Equation XX. In diffusion controlled reaction mechanisms, the rate of product formation decreases proportionally with the thickness, l, of the product barrier layer forming near the surface of the particle, as seen in Figure X

*

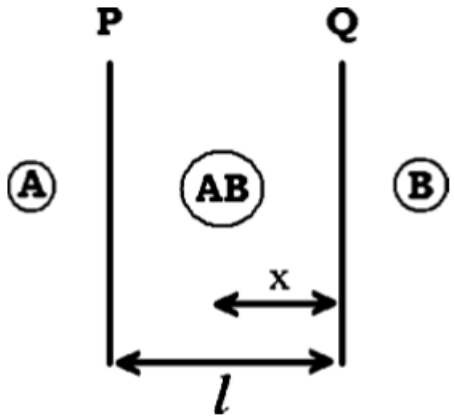

By integrating Fick's law for different geometries and assumptions, one will get different expressions for *g(α)*. The simplest rate equation is obtained for an infinite plane without any shape factor; one-dimensional diffusion, where the conversion fraction α is directly proportional to the layer thickness *l* of product, which is depicted in Figure XX. Applying Fick's law on this regime will yield:

$$\frac{dl}{dt} = -D\frac{M_{AB}}{M_B\rho}\frac{dC}{dx}$$

Here, MAB and MB denote the molecular weights of AB and B respectively, t is time, D is the diffusion coefficient, ρ is the density of the product AB, C is the concentration of B in AB and x is the distance from the border Q into AB. By assuming a linear concentration gradient of B in AB, separating variables and integrating, one will get:

$$l^2 = 2D\frac{M_{AB}(C_P - C_Q)}{M_B\rho}t$$

The factors in front of t can be set to a constant k, which yields the so called parabolic law:

$$l^2 = kt$$

Since α is directly proportional to l, one can write:

$$\alpha^2 = k_2 t$$

where k2 is another constant. Equation XX represents the one-dimensional diffusion, D1, model. When comparing with Equation XX one can see that the expression to the left in Equation YY is *g(α)*, while the constant while k_2 will be the factors in front of t in Equation XX. If instead geometry is based on spherical solid particles as seen in Figure XX, then α can

be expressed in terms of the radii of the particles, *R*, and the spherical thickness *x* of the product layer.

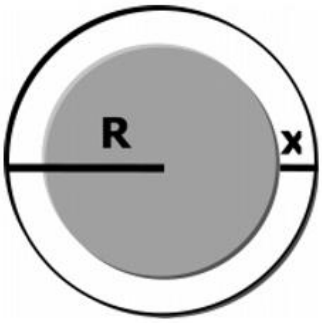

If applying the parabolic law to define x, one will get:

$$(1-(1-\alpha)^{1/3})^2 = k_3 t$$

Equation XX represents the D3, or Jander, model. However, equation XX may be oversimplified because it is derived using the parabolic law which comes from assuming a plane surface. This means that the equation is only valid for low conversion values, i.e. low x/R values, where a near-planar geometry can be assumed. By instead using Fick's law for the radial diffusion in a sphere, while using the same relations between *α*, R and x, and assuming the surface concentration of B to be near equal to zero, one will get:

$$1-\frac{2}{3}\alpha-(1-\alpha)^{2/3} = k_4 t$$

The assumption of zero surface concentration of B comes from assuming that the reaction at the interface happens much faster than diffusion. The model expressed by Equation XX is called the D4, or Ginstling-Brounshtein, model. If instead assuming particles to be cylindrical, where diffusion happens radially through the cylindrical shell, one can derive an alternative D2 diffusion model. By using a similar procedure and the same approximation as for the D4 model, one will obtain the following expression for the D2 model:

$$((1-\alpha)\ln(1-\alpha))+\alpha = k_5 t$$

To get an indication of which of the four reaction diffusion models that could apply for reduction, linear regression was performed in excel where all of the four *g(α)* were calculated for the last reduction step in the Ar/1%O2 cycle program for the first parallel sample of about 20 wt% Fe. The linear regression was forced to go through the origin, id est the b-constant in "y=ax+b" was forced to be zero during analysis, which is a restriction that specifies the

*

model. For the D2 model, one obtained 7 negative values of 1 minus α near α equal to 1, which made $g(\alpha)$ for D2 undeterminable at these points. These points could therefore not be included when performing linear regression.

No previous investigation of the reaction model for reduction of Co-doped-alumina has been done. However, CO_2 oxidation has already been found to follow the F2 reaction-order model, meaning that the reaction rate is proportional to concentration, amount or fraction remaining reactants raised to the power of 2 [47, 48]. A second-order relationship was found to be the best fit for CO_2 concentration, and a 2.4^{th}-order relationship for unreacted solid material [48].

4 PREVIOUSLY REPORTED EXPERIMENTS

4.1 Water splitting cycles

An overview of all of the previously reported hercynite water splitting cycles can be seen in Table 4.1 on the next page. All the experiments were carried out using a stagnation flow reactor (SFR) where the total system pressure was 1 atm. Instead of TGA, MS was used as analysation method, where the amount of hydrogen produced with time was recorded directly. Fe content, yield and rate are given in terms of the total weight of material. All Fe content values are approximations, except for materials prepared by the modified Pechini method, where the materials were analysed by inductively coupled plasma optical emission spectrometry, with all molar ratios reported. The yield per gram Fe is found by dividing the reported yield on the Fe content, and will be a better parameter of comparison, since the Fe content, and thereby active material, varies from sample to sample. Furthermore, one had the following additional conditions:

- The molar ratio of Fe to Co was 2:1 for all the Co-doped-hercynite samples, except for an estimated ratio of 1.4:1 for the one fabricated by the modified Pechini method. The formulas and parameters used to estimate the Fe content and molar ratio of the latter sample is given in Appendix XX.

*

Year	Material	Fabricat-ion method	Fe content [wt%]	T program [°C_{red}(min_{red}) /°C_{ox} (min_{ox})]	Yield [µmol H_2/gt_{ot}]	2s	Peak rate [µmol H_2/g_{tot}·s]	2s	Yield per m_{Fe} [µmol H_2/g_{Fe}]	Number of cycles	Source
2015	$FeAl_2O_4$	Modified Pechini	37.07	1500(60)/ 1350(15)	510	40	1.32	0.07	1375.92	12 (first 6 not reported)	[24, 31]
2015	Co-doped-hercynite	Modified Pechini	17.74	1500(60)/ 1350(15)	310	30	1.64	0.02	1747.91	12 (first 6 not reported)	[24, 31]
2015	$CoAl_2O_4$	Bought pure (≥99%)	0	1500(60)/ 1350(15)	6	10	≈0	[-]	[-]	6	[24, 31]
2014	Co-doped-hercynite	ALD	11.86	1500(60)/ 1350(15)	354	[-]	≈1.1	[-]	2984.93	>200	[26]
2014	Co-doped-hercynite	ALD	11.86	1450(60)/ 1350(15)	198	[-]	≈0.6	[-]	1669.54	>200	[26]
2014	Co-doped-hercynite	ALD	11.86	1400(60)/ 1350(15)	166	[-]	≈0.5	[-]	1399.71	>200	[26]
2014	Co-doped-hercynite	ALD	11.86	1350(60)/ 1350(15)	98	[-]	≈0.2	[-]	826.34	>200	[26]
2013	Co-doped-hercynite	ALD	9.43	1350(60)/ 1000(25)	31.4	2.3	0.06	0.04	333.13	>150 (first 150 not reported)	[5, 8]
2013	Co-doped-hercynite	ALD	9.43	1350(60)/ 1200(25)	93.7	19.2	0.32	0.01	994.09	>150 (first 150 not reported)	[5, 8]
2013	Co-doped-hercynite	ALD	9.43	1350(60)/ 1350(25)	102	18	0.55	0.16	1082.15	>150 (first 150 not reported)	[5, 8]
2013	Ceria	[-]	[-]	1350(60)/ 1000(25)	16.4	3.6	0.14	0.04	[-]	>150 (first 150 not reported)	[5, 8]

Table 4.1: Previously reported water splitting results. *2s* denotes the reported double standard error for values to left of these columns, while [-] means not mentioned, or not applicable.

- 50 V% H_2O at oxidation
- 2013: Reductive flow of He at 100 sccm. However, a 200 sccm flush of He was used for 1 min after oxidation to remove O_2, before the flow was reduced to 100 sccm. At oxidation, 100 sccm He, with equal flow of H_2O, was used.
- 2014 – 2015: Reductive flow of He at 300 sccm. At oxidation, 200 sccm He, with equal flow of H_2O, was used. No flush sequence is reported.

4.2 CO_2 splitting cycles

No total yields for CO_2 cycles have yet been reported, since the focus for investigations performed to this point seems to kinetical studies. However, a peak rate of approximately 0.51 $\mu mol/g_{tot} \cdot s$ have been reported for a CO_2 cycle program with similar conditions as in this work:

- Isothermal cycles at 1400 °C, with 30 min reduction and 20 min oxidation.
- About 46 V% CO_2.
- Material: Co-doped hercynite synthesised by ALD. Molar ratio of Fe to Co was 2:1, with 21.89 wt% Fe (see Appendix XX). The samples were cycled “many” times before use.
- A total flow of 500 sccm at all times.
- Same testing method as for the reported water splitting cycles.

Comparing rates is assumed to be too inaccurate for the cycles run in this work, as the rates seemed to vary too much to be able to extract data, and some examples are seen in Appendix YY.

*

4.3 Oxidation in O_2

Few experiments have also been carried out using free oxygen, but a yield of 100 μmol O_2/g_{tot} has been reported by Weimer et. al. [35] for a non-isothermal program of 25 cycles with an ALD synthesised material, using a 2 °C/s ramp rate from 1000 °C up to 1460 °C in a constant 0.1 V% O2 atmosphere. This corresponds to an equivalent yield of 200 μmol H_2 or CO/g_{tot}. The samples contained 20 wt% $CoFe_2O_3$, which corresponds to 4.76 wt% Fe. When dividing the equivalent yield with m_{Fe}/m_{tot}, one gets 4201.29 μmol H_2 or CO/g_{Fe}. Reduction started at about 1150 to 1200 °C, but not before about 1250 °C when a 16 °C/s ramp rate was used.

5 CHARACTERISATION

5.1 X-ray diffraction analysis

Calcined samples at 300 °C and 1000 °C, together with a reduced and cycled sample as described in Section XX, was analysed by X-ray diffraction (XRD). This is a common method for identifying and quantifying crystalline phases within a material, and can be found described in detail by for instance Klug and Alexander. In general, X-ray beams of a certain wavelength, λ, are sent towards the sample surface at different angles to the surface, θ, and the detected reflections makes it possible to determine the spacing, d, between the lattice planes in the material by Bragg's law [49]:

$$2d \sin\theta = n\lambda \qquad (0.5)$$

n is the order of reflection, and could be any integer. When an array of beams is sent towards the sample, the reflected electromagnetic radiation waves cancel each other out in most directions by destructive interference. However, at some at some points, they add up constructively, maximising each other, which is when n is equal to any integer. d can be calculated by the angles yielding maximum intensity, which allows for phase identification. The principle is illustrated in Figure XX.

*

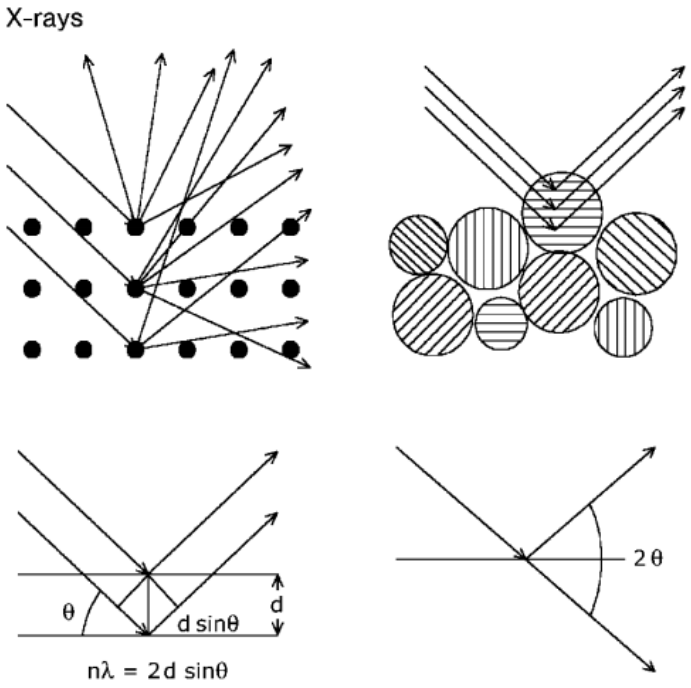

As seen in the upper right corner of Figure XX, the diffraction pattern of a polycrystalline powder at only two-dimensional angles will only constitute from a small fraction of the particles. Thus, rotation of the sample during measurement is important. Different crystalline phases will have peaks at different angles, which can be identified by comparing intensity versus 2θ with a database of standard material XRD patterns. For initial qualitative analysis, one is just comparing peak positions as peak intensity relies on other factors than solely material phases that are present [49].

The XRD profile spectra were obtained by using a Bruker D8 Advance DaVinci X-ray Diffractometer (Bruker Corporation). All samples were prepared in standard sample holders, except from the sample cycled and reduced at 1400 °C, and the sample containing about 10 wt% Fe calcined at 1000 °C, which were prepared in Si crystal with cavity holders. A program of 2θ between 15 – 75° and a constant divergence slit angle of 0.3° was used, with 0.750 second steps with an increment of 2θ of approximately 0.01329° for 1 hour. The search for possible phases present were performed using the DIFFRAC.EVA software (Bruker Corporation), where the PDF-4+ 2015 database (International Centre for Diffraction Data) was used as a reference. Only compounds from Equation XX with the exact same molecular formula, and with a clear, visible match was added to the stacked XRD plots found in Section XX, as well as expected forms of alumina explained in Section XX. CoO was also tested, but where not included because of an apparent poor match. The XRD pattern of Co-doped-

hercynite like in Equation XX will be a mix of the one for hercynite and the one for $CoAl_2O_4$ [24]. For sample only calcined at 300 °C, it is assumed that one will have Fe_2O_3 and Co_3O_4. Nonetheless, there was a poor match for Fe_2O_3, but a seemingly good match for Fe_3O_4, as seen in Figure XX, so this was included instead.

Previously recorded data for pure α-alumina made at NTNU was included in one of the plots that was made. For this sample, a program of 2θ between 20 – 105° and a constant divergence slit angle of 0.2° was used, with scanning for 1 hour.

A previous XRD plot of Co-doped-alumina synthesised by the modified Pechini method, which was explained in Section XX, after water splitting cycles and is seen in Figure XX [31]. The experimental conditions are given in Section XX, but it is not known whether the plot is of reduced or oxidised material.

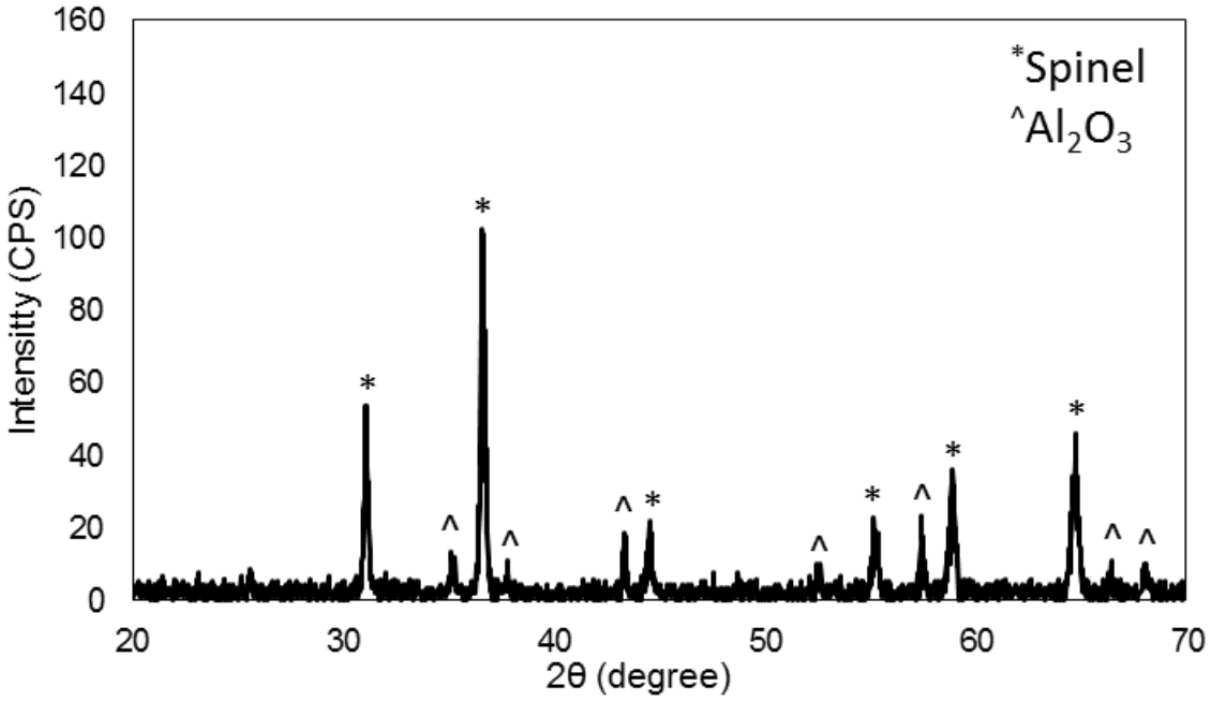

Muhich et al. also did a continuous high temperature XRD (HT-XRD) analysis during CO_2 splitting cycles. During the cycles, $CoFe_2O_4$, which is predicted by Equation XX, was not detected and the Al_2O_3 peak intensity did not change significantly between reduction and

*

oxidation. In theory, assuming a significant reaction extent, much less free alumina should be present after reduction, which can be seen by looking at Equation XX. These results support the theory of a non-stoichiometric mechanism for Co-doped-alumina [24].

5.2 Nitrogen adsorption and desorption analysis

The specific surface area of calcined samples at 300 °C and 1000 °C respectively was estimated by the Brunauer-Emmett-Teller method (BET), while pore volume and diameter was approximated by the Barrett-Joyner-Halenda method (BJH). The BET method was originally described by Brunauer et. al. in 1938, while the BJH method was first reported by Barrett et. al. in 1951. Surface area is estimated by determining amount adsorbed of an appropriate, non-corrosive adsorbate, typically liquid N_2 at about 77 K, at different pressures. As the pressure increases, adsorption of one single monolayer of molecules at the surface will happen first before multilayer physisorption occurs. The surface area is determined by using linear regression in the section where volume uptake increases proportionally with pressure, which is where chemisorption occurs, and is called the BET isotherm. Surface area can be determined from the volume of gas occupying the monolayer, which can be estimated from the BET equation for the linear BET isotherm [50]. The pore volume and pore size distributions can be determined inter alias by further analysis of the desorption data, as pressure is decreased again after adsorption.

There are, however, certain assumptions and limitations for the BET and BJH methods. For example, the heat of adsorption needs to be near-constant over the whole surface, and the assumptions used are strictly not valid for microporous particles. However, in favourable cases, the external area of microporous solids can still be approximated [51]. Furthermore, as a rule of thumb, one needs at least 20 m^2 of total surface to obtain reliable results. Although γ-alumina is a porous structure with medium to large pore sizes, the heat of adsorption is not necessarily constant on all of the surface. Moreover, as explained in Section XX, the surface area and amorphous character of γ-alumina is expected to decrease when calcined at high temperatures. Thus, BET and BJH might not be suitable to characterise these samples.

The adsorption/desorption measurements were done by using a Micromeritics TriStar 3000 instrument (Micromeritics Instrument Corporation) with liquid nitrogen, and the results were retrieved directly from calculations performed by the instrument's software program. All samples were heated to 200 °C in the instrument tubes under vacuum and left to degas at his temperature overnight before analysis. The weights of the samples were recorded after degassing, and was the only manual input parameter required in the software program. The weight of each sample were 50 – 100 mg, which is recommended for the instrument.

Only one previously reported case of BET surface area measurement for Co-doped-hercynite was found, which is from the pure O_2 program described in the end of Section XX. Measured surface area for material synthesised by ALD had an initial surface area of 44 m^2/g, before shrinking to 1.6 m^2/g after cycling. This, together with field emission scanning electron microscopy (FESEM), was used to confirm loss of porosity and sphere volume as the surface area is reduced during cycling. At the same time, they noticed that the oxygen capacity did not decrease after the first cycle, where the assumed structural changes were believed to occur. This may imply that the activity of the material is unaffected by the loss of internal surface area.

*

6 EXPERIMENTAL RESULTS

6.1 Thermogravimetric analysis

6.1.1 Overview

An overview of the average weight change, $m_{change,av}$, observed for the different redox cycle programs specified in Section XX, together with corresponding yields of H_2 or CO are given in Table XX. Equivalent yield is the production capacity assuming all of the weight change is due to loss or addition of oxygen from CO_2 or O_2, and if the weight change had been the same for H_2O as for O_2. This yield is given in terms of amount of dry redox material without organic impurities, as it is clear from Figure XX-YY that one will have water evaporation and eventual combustion of organic impurities in the beginning. The yield per gram Fe is found by dividing the yield on the Fe content, and will be a better parameter of comparison, since the Fe content, and thereby active material, varies from sample to sample. Parameters and formulas used for calculating all of the values are found in Appendix XX.

The first two cycles in Table XX were the non-isothermal ones described in Section XX, using about 50 V% O_2 at oxidation. The number of reduction-oxidation cycles run continuously for each program is given by the numbers in front of the program specifications in the "Cycles" column. "6 Ar/1%O2" means, for instance, the cycle program where 6 redox cycles starting with Ar, since Ar is stated first, and ending with the custom-made gas containing 1 mol% O2, were run continuously. The program specifications are explained in

Cycles	Sample	$m_{change, av}$ [wt%]	2s	Equivalent yield [µmol H_2 or CO/$g_{tot,dry}$]	2s	Yield per m_{Fe} [µmol H_2 or CO/g_{Fe}]
O2 after Ar	20 % Fe (II)	0.60	[-]	377.28	[-]	2102.68
Ar after 1 Ar/O2	20 % Fe (II)	1.10	[-]	687.53	[-]	3831.79
6 Ar/air	10 % Fe	0.19	0.12	130.41	78.80	1363.80
6 Ar/air	20 % Fe	0.48	0.12	318.61	78.29	1773.50
6 Ar/air	20 % Fe (II)	0.37	0.12	247.89	80.40	1381.58
6 Ar/air after 6 Ar/air	20 % Fe	0.53	0.12	340.92	77.10	1897.72
6 Ar/CO2	10 % Fe	0.07	0.02	49.06	10.87	513.05
6 Ar/CO2	20 % Fe	0.14	0.01	96.35	9.50	536.31
6 Ar/CO2	20 % Fe (II)	0.14	0.01	91.53	4.97	510.11
6 Ar/1%O2	20 % Fe	0.46	0.03	320.28	20.79	1782.83
6 1%O2/Ar	20 % Fe	0.43	0.03	303.42	18.16	1688.98
5 1%O2/Ar	20 % Fe*	0.43	0.02	298.72	15.65	1662.81

"10 % Fe" denotes the sample prepared with about 10 wt% Fe, "20 % Fe" signifies the first parallel of about 20 wt% Fe made, and "20 % Fe (II)" means the other parallel, as described in Section XX. For "20 % Fe (II) *", more sample than recommended was used.

*

6.1.2 Non-isothermal TGA program for 20 wt% Fe (II)

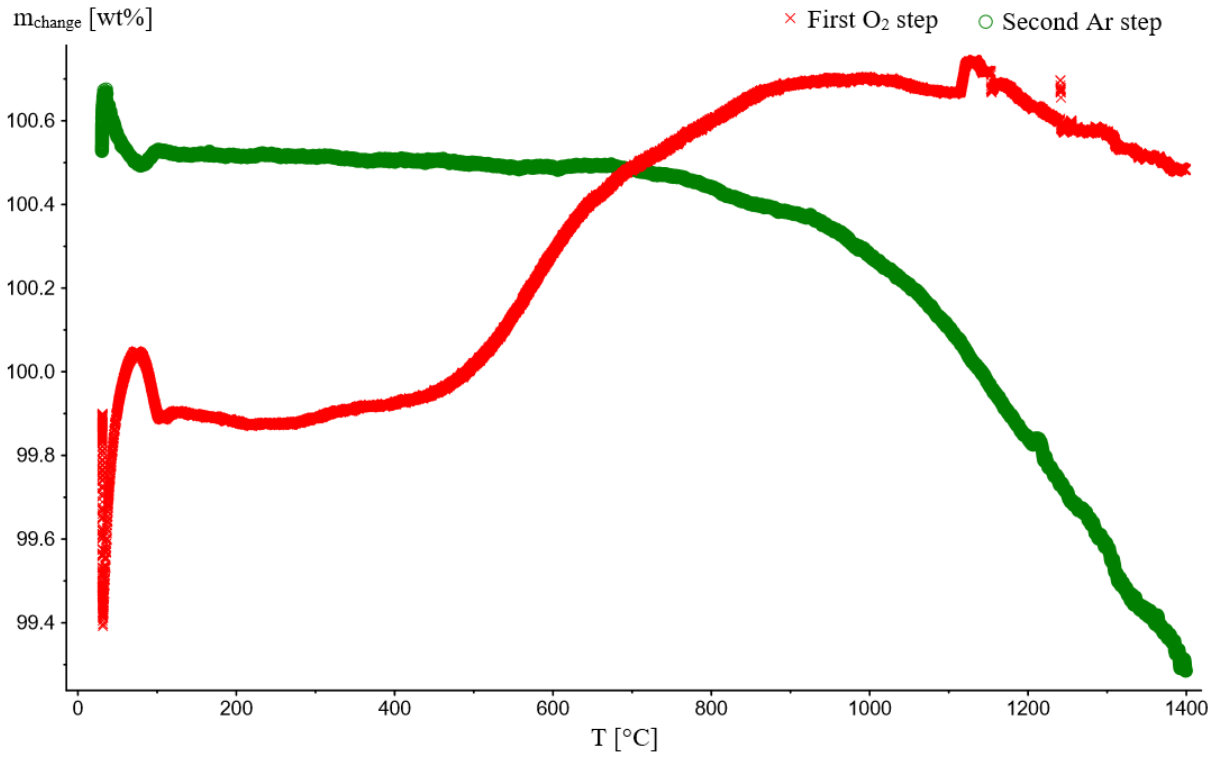

Figure XX shows the two last non-isothermal, or dynamic, TGA program sections for the second parallel of sample containing about 20 wt% Fe; "20 wt% Fe (II)", as explained in Section XX. In these sections, the temperature, *T*, was raised from about 30 °C to 1400 °C with a ramp rate of 5 °C/min, and the program specifications together with plots of all measured values are found in Appendix XX-YY. The program specifications are also explained in Section XX. Measured weight normalized to percent of the initial measured weight is denoted by m_{change}. Red crosses signify the first dynamic program run in 50 V% O_2, while the green circles apply for the second dynamic program run in pure Ar, which are two separate runs. After each run, the sample cooled down to room temperature before it was weighted again manually on an analytical balance. The first Ar run was omitted here, but can be seen in Appendix XX.

6.1.3 Ar/air redox cycles at 1400 °C

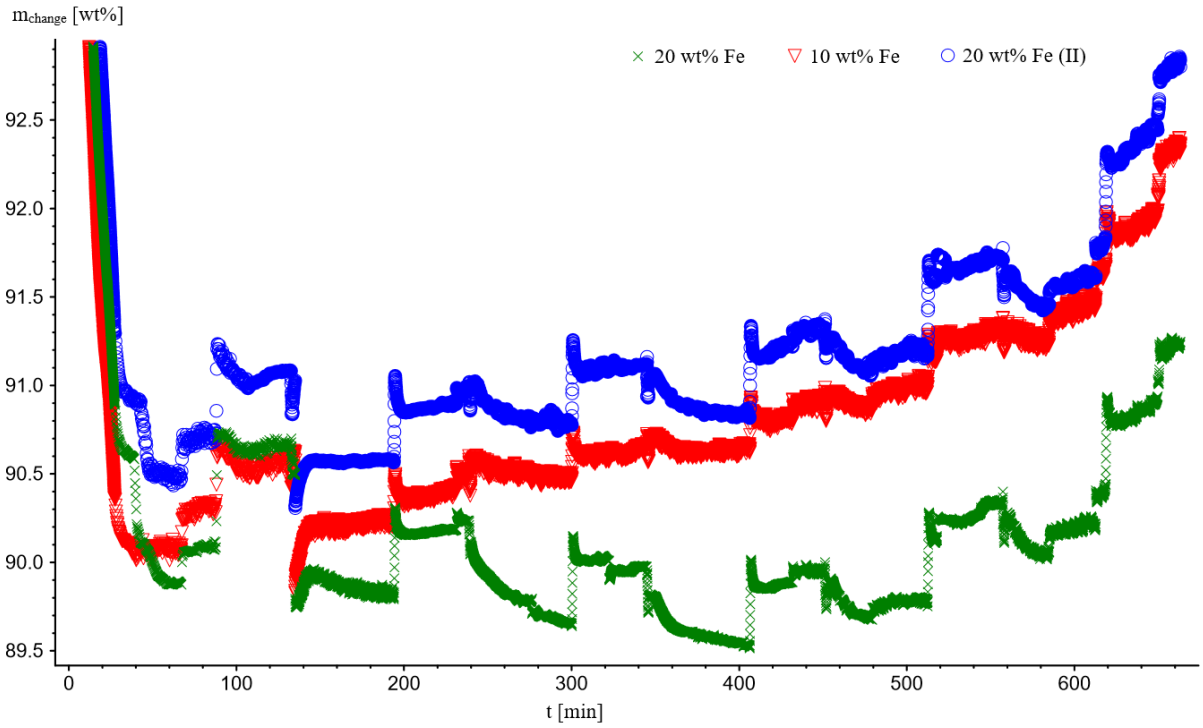

In Figure XX, one can see the lapse of the TGA program for isotherm pressure swing cycles at 1400 °C when using approximately 1 V% O_2 provided by mixing synthetic air with Ar purge flow, as explained in Section XX and YY. Measured weight at a certain time, *t*, normalized to percent of the initial measured weight is denoted by m_{change}. Green crosses represent the first parallel of sample made with approximately 20 wt% Fe, red triangles apply for the one made with about 10 wt% Fe, and the blue circles denote the second parallel made of about 20 wt% Fe, as explained in Section XX. The program specifications together with plots of all measured values, except one of the purge flow rates, are found in Appendix XX-YY.

*

6.1.4 Second run of Ar/air redox cycles at 1400 °C for 20 wt% Fe

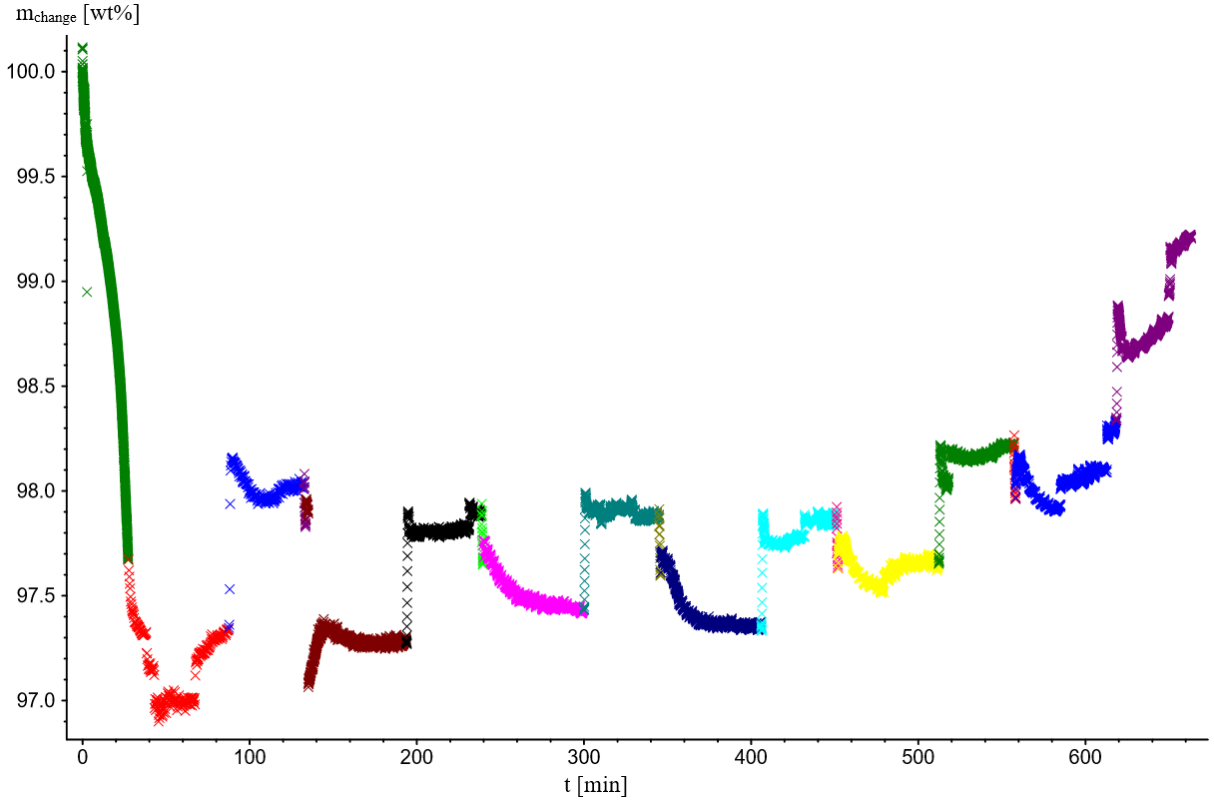

After the cycle program shown in Figure XX, the program was repeated for the "20 wt% Fe" parallel. After the first run, the sample cooled down to room temperature and was weighted again manually on an analytical balance before starting the second run. All switches between different program sections can be distinguished by change of colour in the figure. The program specifications together with plots of all measured values, except one of the purge flow rates, are found in Appendix XX-YY.

6.1.5 Ar/CO_2 redox cycles at 1400 °C

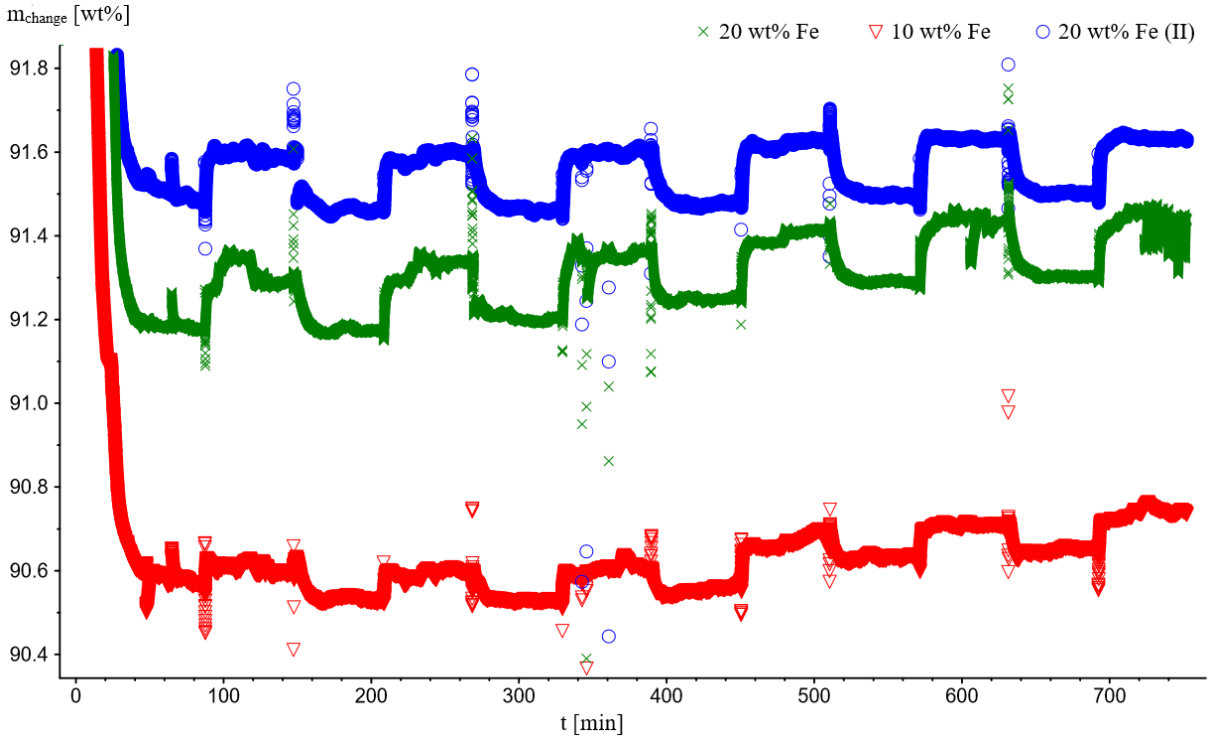

In Figure XX, one can see the lapse of the TGA program for isotherm pressure swing cycles at 1400 °C when using approximately 50 V% CO_2, as explained in Section XX and YY. Measured weight at a certain time, *t*, normalized to percent of the initial measured weight is denoted by m_{change}. Green crosses represent the first parallel of sample made with approximately 20 wt% Fe, red triangles apply for the one made with about 10 wt% Fe, and the blue circles denote the second parallel made of about 20 wt% Fe, as explained in Section XX. The program specifications together with plots of all measured values, except one of the purge flow rates, are found in Appendix XX-YY.

*

6.1.6 Ar/1%O_2 and 1%O_2/Ar redox cycles at 1400 °C for 20 wt% Fe

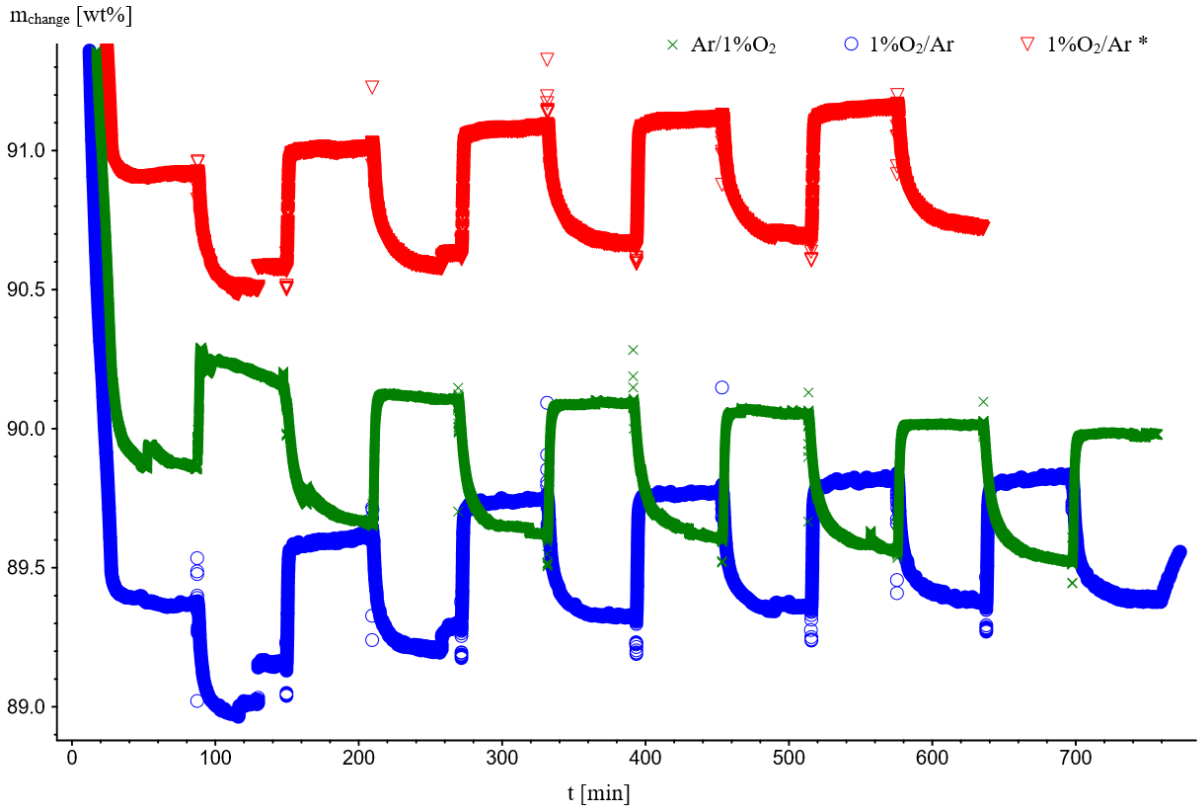

In Figure XX, one can see the lapse of the TGA program for isotherm pressure swing cycles at 1400 °C when using approximately 0.5 V% O_2 provided by a custom-made gas cylinder, as explained in Section XX and YY. Measured weight at a certain time, *t*, normalized to percent of the initial measured weight is denoted by m_{change}. All runs seen are for first parallel of sample made with approximately 20 wt% Fe, but running an oxidation step first and ending with a reduction step was tried for the runs marked with blue circles and red triangles. For the cycle program marked with red triangles, "1%O_2/Ar *", more sample than recommended was used. Cooling for these two runs was also performed with Ar purge to ensure reduced sample for analysis. As one can see for "1%O_2/Ar," the weight seems to increase during cooling although no oxygen should be present. For "1%O_2/Ar *", the cycle program was stopped right before the oxidation step after closing the purge valve to the custom-made bottle with 1 mol% O_2. The weight recorded manually at 1280 °C was 91.38 wt%, and the weight seemed to increase gradually. At 841 °C, the weight had increased to 91.41 wt%. These observations are discussed in Section XX.

The half of a “Ar/1%O2” program was run with an empty crucible to test the accuracy of the TGA method, and the TGA plot be found in Appendix A. A weight change of maximum 0.1 wt% was observed for the first cycle, while the weight change seemed unaffected when switching gases in the two last cycles, as seen in Figure X and Y. The other program specifications together with plots of all measured values, except one of the purge flow rates, are also found in Appendix XX-YY.

6.2 X-ray diffraction

The stacked XRD plots made from the raw data measurements by using DIFFRAC.EVA, as described in Section XX, are found below.

6.2.1 Calcination at 300 °C

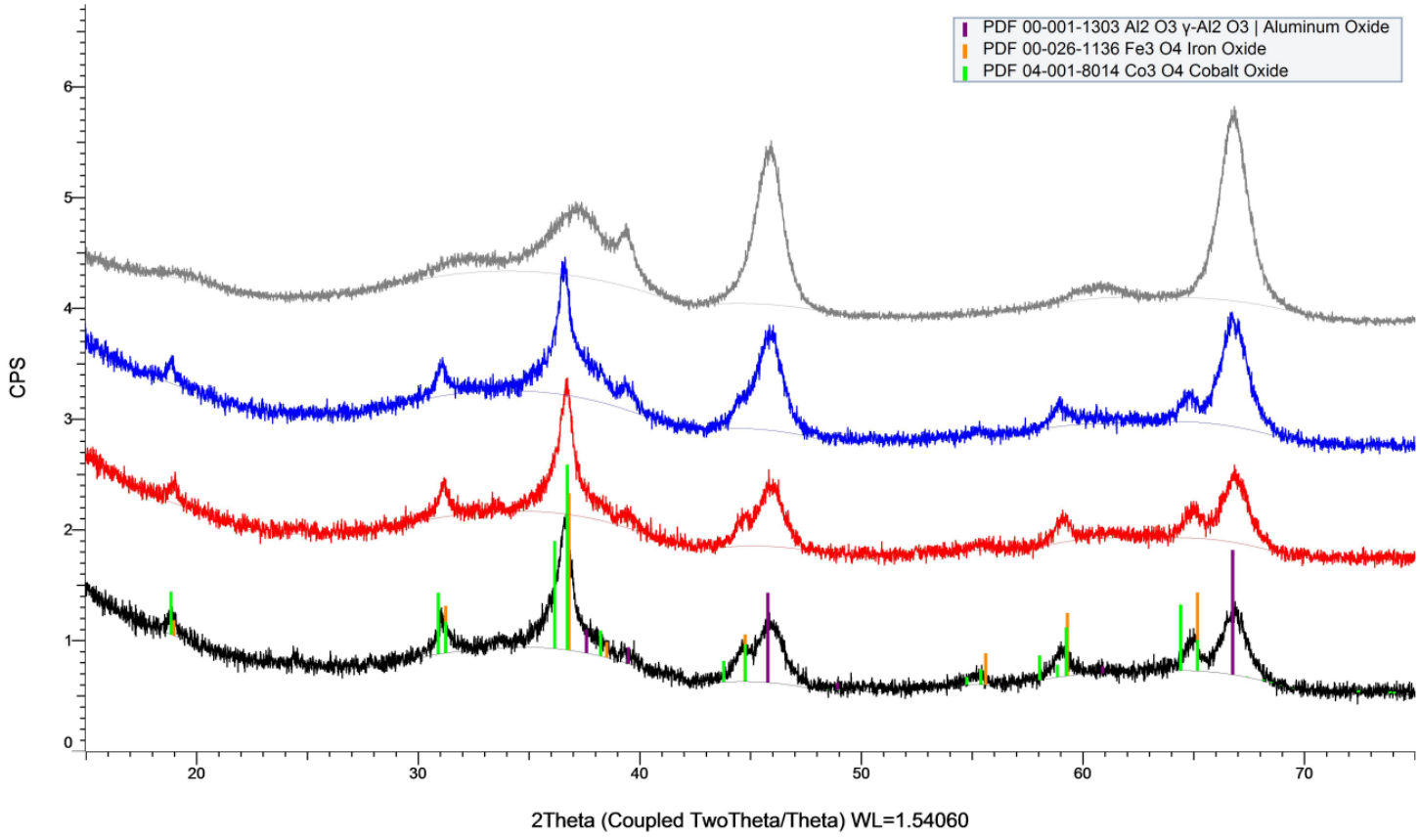

Figure XX shows a stacked plot of all the samples calcined at 300 °C, together with pure, dried and sieved alumina calcined at 500 °C in grey at the top. The bottom black plot in

*

Figure XX is for first parallel of sample made with approximately 20 wt% Fe; “20 % Fe”, the red graph number 2 from the bottom is from the second parallel made of about 20 wt% Fe; “20 % Fe (II)”, and the second upper blue graph is the sample prepared of around 10 wt% Fe; “10 % Fe.” Selected standard patterns are marked with other colours in the figure, which is explained in Section XX.

6.2.2 Calcination at 1000 °C

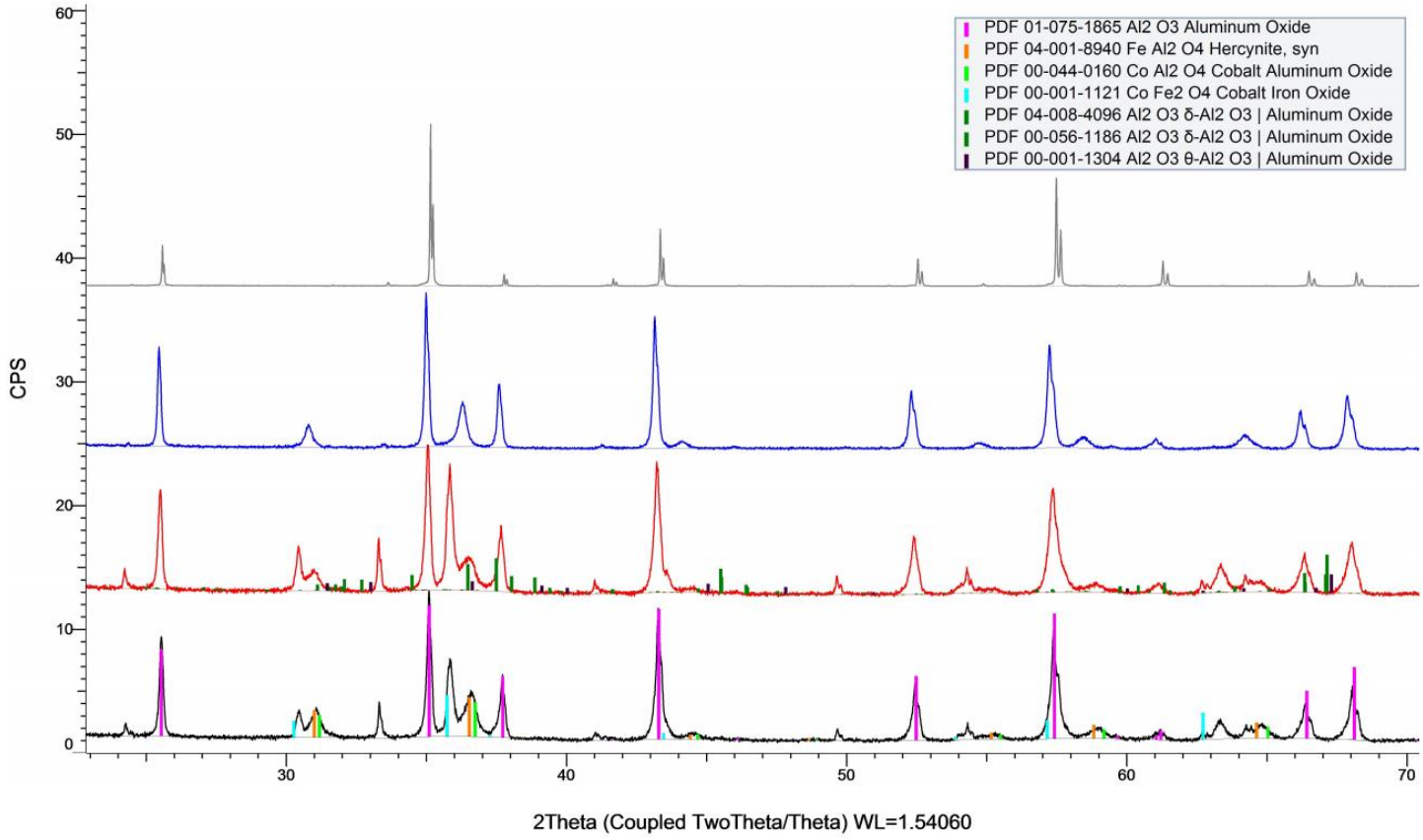

Figure XX shows a stacked plot of all the samples calcined at 1000 °C, together with pure α-alumina previously measured at NTNU in grey at the top. The bottom black plot in Figure XX is for “20 % Fe”, the red graph number 2 from the bottom is for “20 % Fe (II)”, and the second upper blue graph is “10 % Fe”. Selected standard patterns are marked with other colours in the figure, which is explained in Section XX.

6.2.3 20 wt% Fe at different temperatures

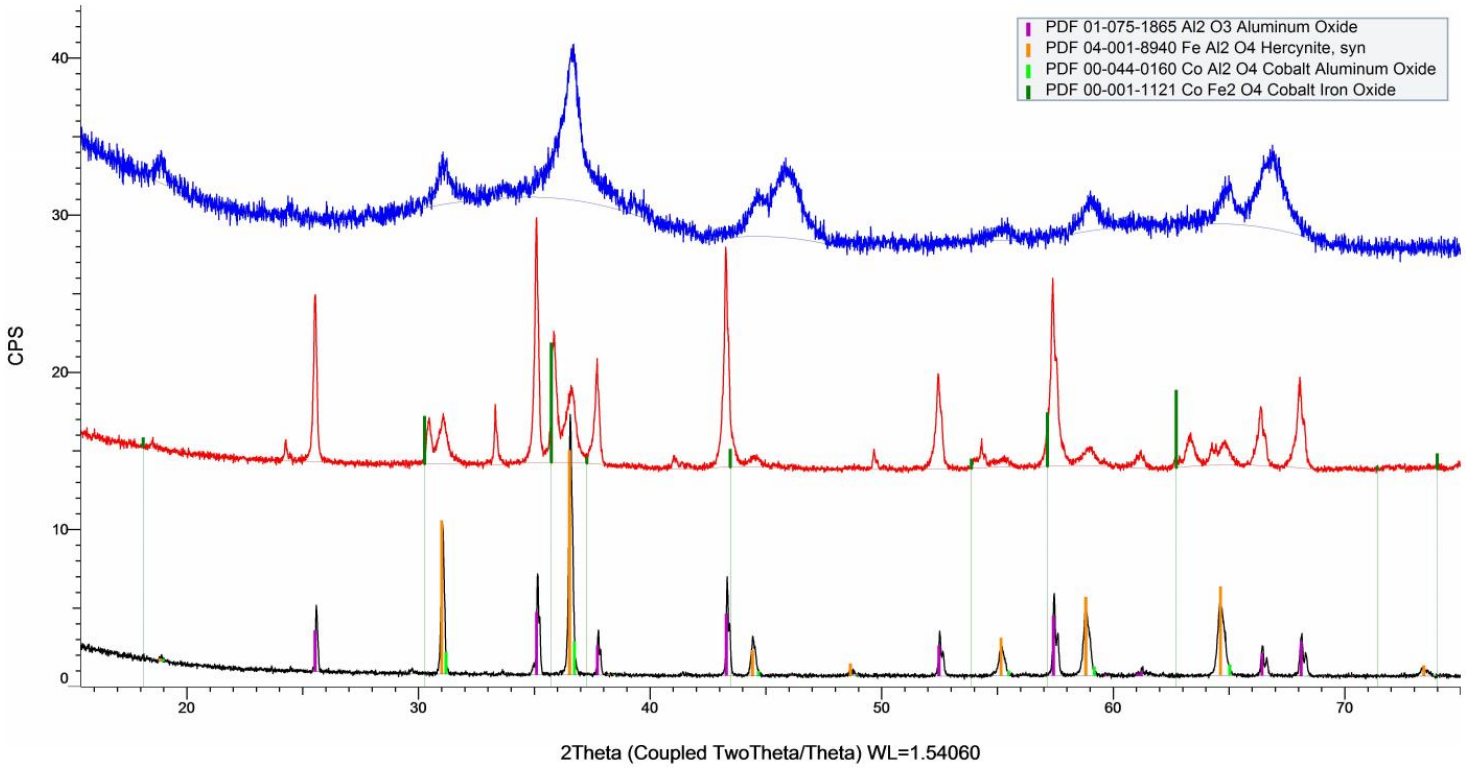

Figure XX shows a stacked plot of "20 % Fe" at increasing calcination temperatures from the top to the bottom. The upper blue graph is sample calcined at 300 °C for more than 16 hours, the middle red one is sample subsequently calcined at 1000 °C overnight together, while the bottom black plot is for reduced sample cycled at 1400 °C for at least 10 hours. Selected standard patterns are marked with other colours in the figure, which is explained in Section XX.

*

6.3 Nitrogen adsorption and desorption

The results from the nitrogen adsorption and desorption analysis explained in Section XX are found in Table XX below. The calcination temperatures and approximate wt% Fe are denoted for the samples, and the details regarding preparation can be found in Section XX. Adsorption/desorption curves, BET surface area reports and pore size distributions retrieved from the analysis software are given in Appendix XX. The uncertainties of the BET surface area values calculated by the program are chosen to be excluded, because they will be misleading, which is discussed in Section XX. The actual BET surface areas and BJH desorption pore volumes are believed to be about 10 % greater than the reported ones at the most.

Sample	BET surface area [m^3/g]	BJH desorption pore volume [cm^3/g]	BJH average pore width [nm]
10 wt% Fe, 300 °C	199.13	0.68	10.59
20 wt% Fe, 300 °C	220.03	0.68	9.71
20 wt% Fe (II), 300 °C	165.18	0.52	10.50
10 wt% Fe, 1000 °C	8.14	0.031	22.50
20 wt% Fe, 1000 °C	10.51	0.065	27.89

6.4 Kinetical study

To get an indication of which of the four reaction diffusion models described in Section XX that could apply for reduction, linear regression was performed in excel where all of the four integrals $g(\alpha)$ of the reaction models were calculated for the last reduction step in the Ar/1%O2 cycle program for the first parallel sample of about 20 wt% Fe. The linear

regression was forced to go through the origin, id est the b-constant in "y=ax+b" was forced to be zero during analysis, which is a restriction that specifies the model. For the D2 model, one obtained 7 negative values of 1 minus α, where α is the conversion fraction, near α equal to 1, which made $g(\alpha)$ for D2 undeterminable at these points. These points could therefore not be included when performing linear regression. The results from the analysis are listed in Table XX.

Diffusion model	k [min^{-1}]	2s [min^{-1}]	R^2
D1	$2.15 \cdot 10^{-2}$	$6.31 \cdot 10^{-5}$	0.93
D2	$1.94 \cdot 10^{-2}$	$3.99 \cdot 10^{-5}$	0.96
D3 (Jander)	$2.15 \cdot 10^{-2}$	$8.54 \cdot 10^{-6}$	0.99
D4 (Ginstling-Brounshtein)	$5.76 \cdot 10^{-3}$	$8.42 \cdot 10^{-6}$	0.98

In Table XX, k is the estimated rate constant of diffusion for the different diffusion model equations, with s denoting estimated standard error for k and where R^2 is the coefficient of determination. A plot of α as a function of time t is given in Figure XX below, with α predicted by the 3D model Equation XX, given the appurtenant estimated k, included.

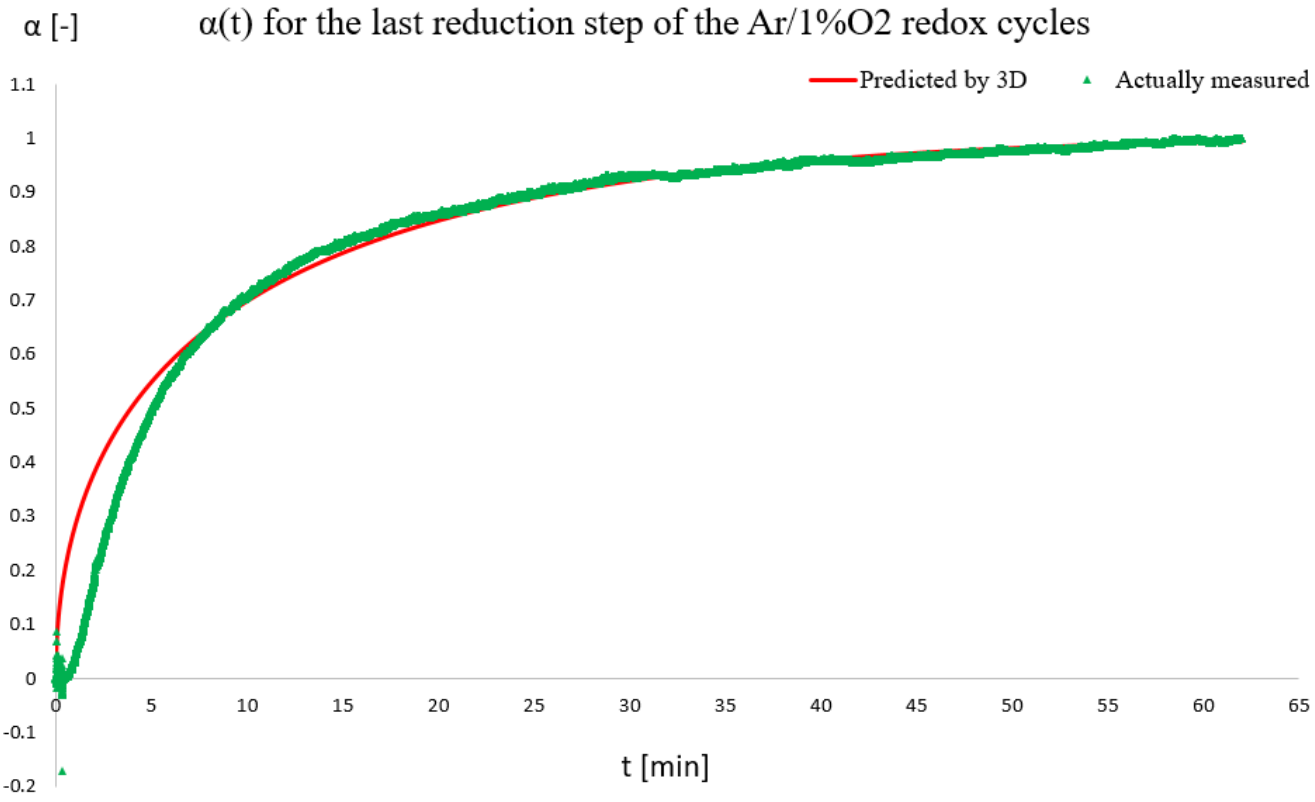

Green triangles on Figure XX above denote α calculated directly by Equation XX. α projected analytically by the 3D model Equation XX, given the appurtenant estimated k, is seen as a red line.

7 DISCUSSION

7.1 Test results

7.1.1 Comparison of sample yields

As seen in Table XX, all estimated theoretical yields for the isothermal cycle programs with respect to wt% Fe were greater for “20 % Fe”; the first parallel of about 20 wt% Fe made, than for the other samples, irrespective of cycle type. The yields with respect to wt% Fe for the second parallel of about 20 wt% Fe, “20 % Fe (II),” and the sample containing about 10 wt% Fe, “10 % Fe,” were more equal to each other. For the case of “20 % Fe (II)”, the lower yield could be related to the improper implementation of the incipient wetness technique (IWT), as explained in Section XX. After being dried overnight, “20 % Fe (II)” had become very stiff, which indicates poor penetration into the pores. Moreover, since the calcination reactor seemed more blackened from the second parallel than the first one, it is suspected that less metal was absorbed in total for “20 % Fe (II)”. When it comes to “10 % Fe,” the lower yield may simply be due to a lower weight fraction of Co. This hypothesis can be supported from previously reported results. As seen for the two upper values in Table XX, the yield per mass Fe is greater for Co-doped-hercynite than for the pure hercynite, given equal testing conditions and fabrication methods. In this case, the peak production rate for Co-doped-hercynite was also greater than for pure hercynite, which was actually predicted by Muhich et. al. They claim that Co can catalyse the surface reaction as well as increasing the rate of O^{2-} anion diffusion through the bulk material [24]. The clear differences observed in terms of

*

higher yield per mass Fe, however, imply that the presence of Co promotes not only reaction rate, but total redox capacity as well.

7.1.2 Comparison of program cycles

The estimated yields for "20 % Fe" using both air and custom-made gas as explained in Section XX are very close to each other. However, the calculated standard errors for the first isothermal cycle programs are very big, because of the big variance in measured weight change, which can be visualized by looking at Figure XX. The reason might be because a higher flow rate than recommended was used for these experiments, as mentioned in Section XX. As seen in Appendix A, the observed weight change profile for the correction program for the "Ar/air" experiment, where cycles were run for empty crucibles, seems to be much more unstable than for the other isothermal cycle experiments. The unexpected steadily weight gain towards the end as seen in Figure XX could be related to the corresponding decrease in in Figure XX for the correction program for empty sample. No significant differences in nitrogen MS signal were detected for the separate runs, as seen in Appendix XX, indicating less likelihood for a leak to have occurred. Nevertheless, weight change variances and fluctuations can also be seen to be present for the "Ar/CO2" program, as seen in Figure XX, even though recommended rates were used here. The fluctuations are particularly dominant in the oxidation steps. This could may be related to that reduction could happen simultaneously with oxidation at elevated temperatures, as mentioned in Section XX. This would be most predominant when using CO_2, because it is harder to split CO_2 than just oxidising the material with free O_2, because of strong interatomic bonds in CO_2.The small increase and decrease observed in Figure XX of the "Ar/CO2" correction program may be due to carbonization, which if present would certainly lead to process complications for solar thermal splitting of CO_2. The most stable and expected profiles were obtained from the last cycle programs, visualised in Figure XX, and results from these cycles are therefore used in the kinetical study, as seen in Section XX.

As expected, all yields are significantly smaller for CO_2 cycles than the cycles where free oxygen was present, at about 1 V% O_2 when purging synthetic air and Ar, and about 0.5 V% O_2 when purging custom-made gas and Ar, as explained in Section XX. Moreover, starting the programs with the first step and heating in inert Ar seems to have a positive effect on

yield, which can be seen when comparing yield for “6 Ar/air” and “6 Ar/1%O2” with the yield for “6 1%O2/Ar” and “5 1%O2/Ar” for “20 % Fe”. One can read from Table XX that it is about 90 % likely that starting heating and cycling with O_2 rather than Ar lowers average weight change. This is in accordance with theory, as mentioned in Section XX. Starting in inert conditions is believed to speed up formation of metal alumina compounds, because the formation of CoO, which is reactive towards forming metal alumina, is more frequent under inert atmosphere [38].

From Figure XX, one can see that oxidation of Co-doped-hercynite in 50 V% O_2 can start at about 500 °C. Reduction for “20 % Fe (II)” starts to increase significantly as low as at around 1000 °C. The lowest reduction temperature for any two-step metal oxide based solar thermal water splitting cycle reported from earlier work is 1200 °C [24]. A similar decrease is observed in Figure XX of the correction file program, but since this signal is subtracted from the one for the sample, this cannot be used to explain the decrease. However, it could be possible that the lower reduction temperature experienced is due to the prior oxidation in enriched oxygen atmosphere. This could have resulted in a more complete oxidation, which could explain why the highest yields were found for this cycle. As mentioned in the end of Section XX, Weimer et. al. got a theoretical yield of 4201.29 μmol H_2 or CO/g_{Fe} for a similar program, which is near 3831.79 μmol H_2 or CO/g_{Fe} obtained for “Ar after 1 Ar/O_2”. One could also see from their results that reduction occurred at about 1150 to 1200 °C using a ramp rate of 2 °C/s, but not before about 1250 °C when a 16 °C/s ramp rate was used. These rates are much higher than 5 °C/min which was used here, which could also explain the lower recorded reduction temperature. In addition, Weimer et.al. used a constant 0.1 V% O2 atmosphere, while only Ar was flushed during reduction in this work. In addition, it seems like the weight 0.2 % Nonetheless, few non-isothermal cycles were run here, and these observations have to be confirmed by repeated experiments.

The initial Ar run was omitted from Section XX, because active material is believed to be formed during this step, so it does not represent the behaviour of active material. Furthermore, as seen in Figure XX in Appendix A, one cannot distinguish between weight decline due to evaporation or decline due to reduction.

*

7.1.3 Comparison with literature values

The calculated yields using oxidation steps with free O_2 are similar to many of the ones for reported water splitting cycles run at similar conditions, as seen in Table XX. The yield for a 11.86 wt% Fe material of same molar ratio of Fe to Co was for instance 166 μmol H_2 /g_{tot}, while it was calculated to be equivalent to 130.41 +- 78.80 μmol H_2 /g_{tot} for "10 % Fe". This reported cycle was, however, run at 1350 °C for oxidation and 1400 °C for reduction. Two other reported materials with about 10 wt% Fe, with the same molar ratio and preparation method, had a yield of 98 μmol H_2 /g_{tot} and 102 +- 18 μmol H_2 /g_{tot} respectively for isothermal cycling at 1350 °C. However, all the mentioned materials were cycled more than 150 times, and these results are therefore more representative for long-term behaviour. Nevertheless, the Co-doped-alumina of 17.74 wt% Fe prepared by a modified Pechini method was only cycled 12 times, and the yield for this material is reported to be 310 μmol H_2 /g_{tot} for the 6 last cycles. For comparison, "20 % Fe", actually containing no more than 17.96 wt% Fe, was 340.92 +- 77.10 μmol H_2 /g_{tot}, based on the average of "6 Ar/air after 6 Ar/air". For all the other free O_2 cycling programs, a similar yield was estimated for this material. The latter reported material was even cycled at 1500 °C for reduction and 1350 °C for oxidation, which is much better cycling conditions than the isothermal program at 1400 °C, as explained in Section XX. The yield using free O_2 is believed to be greater than for just purging steam, though. As mentioned above, about 100 μmol H_2 /g_{tot} is reported for about 10 wt% Fe for isothermal cycles at 1350 °C, while it was about 50 μmol H_2 /g_{tot} for "10 % Fe" in the "6 Ar/CO2" program. Anyhow, when looking at the total picture, it would be reasonable to claim that the performance in terms of production capacity of the materials made is similar to the performance of other Co-doped-hercynite synthesised earlier.

7.2 Weight increase in the end of the "1%O2/Ar" program

As seen in Appendix A, there is approximately no difference between the N_2 MS signal between the correction file program and "1%O2/Ar" towards the end of the program, which implies that an eventual air leak has to have happened in the exact same manner for both programs, which is unlikely. When looking at Figure XX of the TGA program for the

correction file, there is only a slight weight decrease of less than 0.1 wt%, so the reason for the observed weight increase is unknown. However, the particles that were taken out from the TGA instrument afterwards looked more blue than material calcined at 1000 °C, which was more red. This observation could be explained by reduced surface Fe particles [35].

7.3 DSC signal

When looking at all the TGA reports in Appendix A, one can see that the DSC signal decreases abruptly when switching to oxidation, while the opposite happens when switching to reduction for all programs. This is expected, since oxidation is exothermic, while reduction is endothermic.

7.4 Characterisation

7.4.1 X-ray diffraction

When comparing the different plots in Section XX, the transition towards more crystalline α-alumina is evident. As seen in Figure XX, the higher calcination temperature, the sharper peaks, indicating a more crystalline structure. Surprisingly, as seen in Figure XX, the α-alumina pattern is quite clear already at 1000 °C. At this temperature, one should have δ- or θ-alumina [36, 39, 40], but there seems to be a mismatch from the standard δ- or θ-patterns found in the PDF-4+ 2015 database. At the same time, the α-alumina peaks are fitting perfectly with the data base value, as well as measured values. A possible explanation to this could be that the metal present enables corundum crystal growth at lower temperatures, which is observed when adding fluoride ions for instance [43].

In conformity with the findings of Muhich et. al., no $CoFe_2O_4$ was detected for cycled material. The sample produced here, however, was reduced. Thus, given a high yield and the stoichiometric mechanism in Equation XX, there should be difficult to spot this compound anyways. On the other hand, when looking at Figure XX and YY, there seems to be a possible fit for $CoFe_2O_4$ for sample calcined at 1000 °C, except for “10 % Fe”. It may be that the low

*

calcination temperature leads to an uncomplete reaction towards metal alumina, leading to the formation of pure mixed metal oxide instead. Nonetheless, metal alumina patterns cannot be excluded from fitting the calcined sample at 1000 °C either. Thus, both phases seem to be present for the two parallels of about 20 wt% Fe. The peaks for $CoFe_2O_4$ appear sharper for "20 % Fe (II)" than for "20 % Fe", but further analysis is needed before one can say anything for certain about quantity.

As experienced by Muhich et. al., it is difficult to determine whether separate phases of hercynite and $CoAl_2O_4$ exist rather than a mixed one based on initial XRD analysis, because the XRD pattern for the two phases are very similar, as seen in Figure XX and YY. To determine a mixed phase or not, further analysis would be needed. Muhich et. al. used scanning electron microscopy and energy dispersive X-ray spectroscopy (SEM/EDS) to measure the d-spacing between atoms when they concluded that there is a mixed phase.

The XRD pattern of cycled "20 % Fe" is as good as identical to Figure XX of the previously reported XRD graph for cycled Co-doped-hercynite made by the Pechini method as seen in Section XX, which indicates that the same phases exist in both materials.

7.5 Nitrogen adsorption-desorption

As expected, the surface area and pore volume were found to decrease heavily when calcined at 1000 °C, which is very clear when looking at the values in Table XX. As explained in Section XX, this is related to the phase transition towards α-alumina, which is confirmed by the XRD results. The surface area of "20 % Fe" is calculated to be greater than that of "10 % Fe" for calcination at both 300 °C as well as 1000 °C, and the pore volume for "20 % Fe" is more than double as big as for "10 % Fe" when calcined at 1000 °C. Most commonly, the surface area and pore volume are expected to decrease due to pore plugging [52], and as a result of metal particles occupying some of the pore volume. However, in certain cases, given a well-developed metal-support interaction, added metal can increase intracrystallinity, leading to greater surface area and pore volume [53]. One would also may think that the

nitrate precursors used could have changed the alumina surface, but residue nitrates would most probably have been removed during calcination. Further investigations should be carried out to confirm this phenomenon.

There are, however, certain limitations to the nitrogen sorption method, as mentioned in Section XX, especially for low surface area samples. Nevertheless, a linear trend can be seen in Appendix A, which is required for calculating the surface area. Thus, the assumption of a constant BET isotherm is at least valid, and implies a constant heat of adsorption when the initial monolayer is formed. Moreover, the sorption isotherms seen in Appendix AA resemble a mix between the type III and IV isotherm [54] and both types are suitable for surface area determination by the BET method. The hysteresis is situated well outside the pressure range of the BET plot, which were based on a p/p_o between 0 and 0.2, so the measurement can be assumed to be fairly accurate on this point.

Nevertheless, the actual BET surface areas and BJH desorption pore volumes are believed to be about 10 % greater than the reported ones at the most, because of problems with obtaining the accurate weight of samples. Water or acetone is believed to have been present during initial weighing the sample tubes, since the weight would never stabilise from a slow and steady decrease. At most, the weight error could may be 5 mg. Since the weight of the empty tubes are subtracted from the weight of tubes with sample, it is most likely that one has more sample than recorded. When the initial weight was increased by 5 mg when generating the sorption report for "20 % Fe," both the BET surface area and the BJH desorption pore volume increased by about 10 %.

The previously reported surface area of initially prepared sample by the ALD technique, as mentioned in Section XX, was only 44 m^2/g which is much less than areas for the initially calcined samples seen in Table XX. However, Weimer et. al. do not mentioned under which temperatures ALD has been conducted, but it is typically below 350 °C [29]. For the samples calcined at 1000 °C, the surface area is greater than 1.6 m^2/g reported for cycled material, but as discussed in Section XX, this would be partially due to incomplete conversion to α-alumina.

*

7.6 Kinetic study

The coefficient of determination found for the four different diffusion models for “20 % Fe” are all above 0.9, which means that all models are potentially good fits. It was highest for D3 diffusion, however, and conversion fraction predicted with time can be seen with together with the measured one in Table XX. The D4 model’s coefficient of determination is yet approximately equal to the D3 one. A good fit for D3 indicates low conversion value, where only material near the surface is reacting, as explained in Section XX. Since D4 also is a good fit, it also means that the assumption of zero O_2 surface concentration for D4 could be true, and that the redox material particles are spherical. In further studies, one could do linear regressions for more than one cycle to verify the reaction model.

If isothermal experiments at other temperatures had been run, one could have calculated the frequency factor and activation energy by making an Arrhenius plot of the different obtained reaction rates constants found. It is possible, however, to mix non-isothermal with isothermal calculations since the non-isothermal heating rate was constant, but the non-isothermal data obtained is for the other parallel of 20 wt% Fe and in pure O_2, and it would therefore be incorrect to mix these two.

8 CONCLUSION

Successfully tested and characterised Co-doped-hercynite redox material was synthesised by the incipient wetness technique (IWI), with theoretical production capacities of H_2 or CO per mass Fe similar to the ones of other Co-doped-hercynite produced earlier by atomic layer deposition (ALD) and a modified Pechini method. For isothermal pressure swing CO_2 splitting cycles at 1400 °C using Ar and 50 V% CO_2, the yield of CO was estimated to be 96.35 +- 9.50 μmol CO /$g_{tot, dry}$ at the most based on thermogravimetric analysis (TGA) for 6 initial cycles for Co-doped-hercynite material with about 17.94 wt% Fe. This corresponds to 536.30 μmol CO /g_{Fe}. For equal conditions and material, but when using 0.5 V% O2, the uptake of O_2 was estimated to be 160.14 +- 10.39 μmol O_2 /$g_{tot, dry}$, while it was estimated to be 159.30 +- 39.15 μmol O_2 /$g_{tot, dry}$ when using 1 V% O_2. This corresponds to an average yield of about 889.08 μmol O_2 /g_{Fe}. The activity of this material was confirmed for 12 subsequent 1 V% O_2 cycles. Results and considerations imply that the total yield per mass Fe is dependent on the concentration of Co.

When running a non-isothermal program using 50 V% O_2 and a ramp rate of 5 °C/min, oxidation was observed to start at about 500 °C, and reduction to start at as low as at around 1000 °C. For comparison, the lowest reduction temperature for any two-step metal oxide based solar thermal water splitting cycle reported from earlier work is 1200 °C. Calculated

*

yield per mass Fe for the two runs in O_2 and Ar respectively after an initial run in Ar was near the yield calculated from another reported similar non-isothermal O_2 cycling program.

During CO_2 splitting cycles, weight change fluctuations seemed to occur during oxidation, which could be related to simultaneous reduction activity. Slight weight increase during oxidation and subsequent decrease for reduction for an empty alumina crucible was observed during these cycles only, which could imply carbonization.

Testing procedures were evaluated, and found to be reliable. The most stable and expected runs were performed using custom-made Ar gas with 1 V% O_2. It is about 90 % likely that starting heating and cycling with O_2 rather than Ar lowers average weight change, which is in accordance with theory regarding increasing formation rate of Co alumina compounds when calcination occurs under inert atmosphere. More uncertainty, however, is related to nitrogen sorption characterisation, where exact values and trend of increasing surface area and pore volume the higher metal loading have to be confirmed by further studies. However, samples prepared by calcination at 300 °C is believed to be at least about 200 m^3/g, and at least about 8 m^3/g when calcined at 1000 °C in air.

Results from X-ray diffraction strongly indicated formation of α-alumina for all samples made and calcined at only 1000 °C overnight. For the samples prepared with the highest wt% Fe, $CoFe_2O_4$ could not be excluded of being present, but it was not identified for reduced and cycled material. These observations are, however, not sufficient to invalidate the previously assumed stoichiometric reaction mechanism. Apart from this, the expected phases were identified for all samples at the different calcination temperatures, and the XRD pattern of cycled material was found to be as good as identical to a previously reported cycled Co-doped-hercynite material.

All four diffusion models for reduction kinetics were found to be potentially good fits for reduction kinetics, but D3 and D4 were found to be the best. Further studies are needed to validate this, and to obtain the rate constant parameters for reduction.

*

9 REFERENCES

1. Muhich, C.L., et al., *A review and perspective of efficient hydrogen generation via solar thermal water splitting.* Wiley Interdisciplinary Reviews: Energy and Environment, 2015. **5**(3): p. 261-287.
2. *Which Solar Panels Are Most Efficient?* No date [cited 2016 11. July]; Available from: http://www.theecoexperts.co.uk/which-solar-panels-are-most-efficient.
3. Honsberg, C. and S. Bowden. *Efficiency and Solar Cell Cost*. No date [cited 2016 11. July]; Available from: http://www.pveducation.org/pvcdrom/design/efficiency-and-cost.
4. Christopher Muhich, J.M., K.W. Brian Ehrhart, Darwin Arifin,, and C.M. Ibraheam Al-Shankiti, Alan W. Weimer. *Solar-Thermal Redox-Based Water Splitting Cycles*. DOE Hydrogen and Fuel Cells Program 2014 [cited 2016 11. July]; Available from: https://www.hydrogen.energy.gov/pdfs/progress14/ii_c_1_weimer_2014.pdf.
5. Christopher L. Muhich, B.W.E., Kayla C. Weston, Paul Lichty, Xinhua Liang, and C.B.M. Janna Martinek, Alan W. Weimer. *Supplementary Materials for Efficient Generation of H2 by Splitting Water with an Isothermal Redox Cycle*. 2013 [cited 2016 11. July]; Available from: http://science.sciencemag.org/content/sci/suppl/2013/07/31/341.6145.540.DC1/Muhich.SM.pdf.
6. Rytter, E., et al., *Process concepts to produce syngas for Fischer–Tropsch fuels by solar thermochemical splitting of water and/or CO2.* Fuel Processing Technology, 2016. **145**: p. 1-8.
7. May, J. *The Fischer-Tropsch Process and Its Influence*. 2002 [cited 2016 13. Jan]; Available from: http://stoltz.caltech.edu/litmtg/2002/may-lit-9_26_02.pdf.

8. Muhich, C.L., et al., *Efficient Generation of H2 by Splitting Water with an Isothermal Redox Cycle.* Science, 2013. **341**(6145): p. 540-542.

9. Kromer, M., et al. *Support for Cost Analyses on Solar-Driven High Temperature Thermochemical Water-Splitting Cycles*. 2011 14 Dec 2015]; Available from: https://www1.eere.energy.gov/hydrogenandfuelcells/pdfs/solar_thermo_h2_cost.pdf.

10. Weimer, A.W. and M.M. Channel. *Solar-Thermal ALD Ferrite-Based Water Splitting Cycle*. University of Colorado, Department of Chemical & Biological Engineering 2011 14 Dec 2015]; Available from: http://www.hydrogen.energy.gov/pdfs/progress11/ii_f_4_weimer_2011.pdf.

11. Kim, J., et al., *Fuel production from CO2 using solar-thermal energy: system level analysis.* Energy & Environmental Science, 2012. **5**(9): p. 8417-8429.

12. Sinnott, R. and G. Towler, *Chemical engineering design : principles, practice and economics of plant and process design*. Vol. 5th ed. 2008: Elsevier/Butterworth-Heinemann.

13. Bustamante, F., et al. *KINETIC STUDY OF THE REVERSE WATER GAS SHIFT REACTION IN HIGH-TEMPERATURE, HIGH-PRESSURE HOMOGENEOUS SYSTEMS* 2002 [cited 2016 13 Jan]; Available from: https://web.anl.gov/PCS/acsfuel/preprint%20archive/Files/47_2_Boston_10-02_0274.pdf.

14. *HTI. Ceramic Heat Exchangers - Efficient use of Energy*. [cited 2016 13 Jan]; Available from: http://www.heatxfer.com/files/Ceramic_Heat_Exchanger_Catalog.pdf.

15. Ermanoski, I., J.E. Miller, and M.D. Allendorf, *Efficiency maximization in solar-thermochemical fuel production: challenging the concept of isothermal water splitting.* Physical Chemistry Chemical Physics, 2014. **16**(18): p. 8418-8427.

16. al., J.K.M.e. *High temperature heat exchanger studies for applications to gas turbines*. 2009; Available from: http://link.springer.com/article/10.1007/s00231-009-0560-3.

17. AspenTechnology, *Aspen Energy Analyzer - Reference Guide*. 2014.

18. Hashem, H. *Stellio heliostat set to cut CSP tower costs by 20%*. 2016 [cited 2016 11. July]; Available from: http://social.csptoday.com/technology/stellio-heliostat-set-cut-csp-tower-costs-20.

19. *Stellio Heliostat – the state-of-the-art Concentrating Solar Power (CSP)*. 2015; Available from: http://www.sbp.de/en/themes/stellio-heliostat-the-state-of-the-art-concentrating-solar-power-csp/.

20. Siegel, N.P., et al., *Factors Affecting the Efficiency of Solar Driven Metal Oxide Thermochemical Cycles.* Industrial & Engineering Chemistry Research, 2013. **52**(9): p. 3276-3286.

21. Niekerk, W.v. *Press release, New Solar Resource Maps for South Africa*. 2014 [cited 2016 11 July]; Available from: http://ises.org/fileadmin/user_upload/PDF/Stellenbosch_University__New_Solar_Resource_Maps_for_South_Africa.pdf.

22. *South Africa*. 2016 [cited 2016 11 July].

*

23. *Concentrating Solar Power*. 2012 [cited 2016 11 July]; Available from: http://www.irena.org/documentdownloads/publications/re_technologies_cost_analysis-csp.pdf.

24. Muhich, C.L., et al., *Predicting the solar thermochemical water splitting ability and reaction mechanism of metal oxides: a case study of the hercynite family of water splitting cycles.* Energy & Environmental Science, 2015. **8**(12): p. 3687-3699.

25. Christopher Muhich, B.E., Janna Martinek, Darwin Arifin,, K.Z. Kayla Weston, Rachel Viger, Charles Musgrave,, and A.M. Judy Netter, Aldo Steinfeld, Alan Weimer. *Solarthermal Redox-based Water Splitting Cycles*. 2014 [cited 2016 11. July]; Available from: https://www.hydrogen.energy.gov/pdfs/review14/pd028_weimer_2014_o.pdf.

26. Muhich, C.L., et al. *Near-isothermal Ferrite/Alumina ("Hercynite Cycle") Two-step Red/Ox Cycle for Solar-thermal Water Splitting*. in *Light, Energy and the Environment*. 2014. Canberra: Optical Society of America.

27. Pitchumani, R., et al., *Proceedings of the SolarPACES 2013 International ConferenceAdvancing Oxide Materials for Thermochemical Production of Solar Fuels.* Energy Procedia, 2014. **49**: p. 2019-2026.

28. Alan W. Weimer and M.C. Jonathan Scheffe. 2010 [cited 2016 11. July]; Available from: https://www.hydrogen.energy.gov/pdfs/progress10/ii_f_3_weimer.pdf.

29. Johnson, R.W., A. Hultqvist, and S.F. Bent, *A brief review of atomic layer deposition: from fundamentals to applications.* Materials Today, 2014. **17**(5): p. 236-246.

30. Kayla Weston, C.L.M., Darwin Arifin, Alan W Weimber, Anthony H. McDaniel. *A Method for Clean H2 Generation from Solar Heat and Water*. 2013 [cited 2016 11. July]; Available from: https://aiche.confex.com/aiche/2013/webprogram/Paper350053.html.

31. Muhich, C.L., et al. *Supplementary Information, Predicting the Solar Thermochemical Water Splitting Ability and Reaction Mechanism of Metal Oxides: a Case Study of the Hercynite Family of Water Splitting Cycles*. 2015 [cited 2016 11. July]; Available from: http://www.rsc.org/suppdata/c5/ee/c5ee01979f/c5ee01979f1.pdf.

32. Yahya, N., *Carbon and Oxide Nanostructures: Synthesis, Characterisation and Applications*. 2011.

33. Zha, Y., *The Rational Preparation of Niobia Promoted and Supported Platinum Catalysts*. 2007.

34. Yang, R.T., *Adsorbents: Fundamentals and Applications*. 2013.

35. Alan W. Weimer, D.A. and V.A. Xinhua Liang, Paul Lichty. *Solar-Thermal ALD Ferrite-Based Water Splitting Cycle*. 2012 [cited 2016 11. July]; Available from: https://www.hydrogen.energy.gov/pdfs/progress12/ii_e_4_weimer_2012.pdf.

36. Hudson, L.K., et al., *Aluminum Oxide*, in *Ullmann's Encyclopedia of Industrial Chemistry*. 2000, Wiley-VCH Verlag GmbH & Co. KGaA.

37. Yvan J.O. Asencios, M.R.S.-K. *Synthesis of high-surface-area gamma-Al2O3 from aluminum scrap and its use for the adsorption of metals: Pb(II), Cd(II) and Zn(II)*. 2012 [cited 2016 11. July]; Available from: http://www.producao.usp.br/bitstream/handle/BDPI/41998/wos2012-4261.pdf?sequence=1.

38. M. Rotan, E.R., M.-A. Einarsrud, and T. Grande, *Solid state mechanism leading to enhanced attrition resistance of alumina based catalyst supports for Fischer-Tropsch synthesis.* Journal of the European Ceramic Society, 2013. **33**: p. 1-6.

39. Chorkendorff, I. and J.W. Niemantsverdriet, *Solid Catalysts*, in *Concepts of Modern Catalysis and Kinetics*. 2005, Wiley-VCH Verlag GmbH & Co. KGaA. p. 167-214.

40. Santos, P.S., H.S. Santos, and S.P. Toledo, *Standard transition aluminas. Electron microscopy studies.* Materials Research, 2000. **3**: p. 104-114.

41. Wojciech L. Suchanek, J.M.G.e., Pasquale F. Fulvio, Mietek Jaroniec. *Hydrothermal Synthesis and Surface Characteristics of Novel Alpha*

Alumina Nanosheets with Controlled Chemical Composition. 2010 [cited 2016 11. July]; Available from: http://pubs.acs.org/doi/pdf/10.1021/cm102158w.

42. Suchanek, W.L. *Hydrothermal Synthesis of Alpha Alumina (α-Al2O3) Powders: Study of the Processing Variables and Growth Mechanisms*. 2009 [cited 2016 11. July]; Available from: http://onlinelibrary.wiley.com/doi/10.1111/j.1551-2916.2009.03399.x/full.

43. Karl Wefers, C.M., *Oxides and Hydroxides of Aluminium*. 1987: Alcoa Laboratories.

44. GmbH, N.-G., *STA 449 C Jupiter Operational Manual*.

45. MettlerToledo, *Interpreting DSC curves; Part 1: Dynamic measurements.* UserCom, (11).

46. IUPAC. *Definitions of terms relating to mass spectrometry (IUPAC Recommendations 2013)*. 2013; Available from: http://www.iupac.org/publications/pac/pdf/asap/pdf/PAC-REC-06-04-06.pdf.

47. Flanagan, A.K.a.D.R., *Solid-State Kinetic Models: Basics and Mathematical Fundamentals.* J. Phys. Chem., 2006.

48. Muhich, C.L., et al., *Extracting Kinetic Information from Complex Gas–Solid Reaction Data.* Industrial & Engineering Chemistry Research, 2015. **54**(16): p. 4113-4122.

49. Niemantsverdriet, J.W., *Diffraction and Extended X-Ray Absorption Fine Structure (EXAFS)*, in *Spectroscopy in Catalysis*. 2007, Wiley-VCH Verlag GmbH & Co. KGaA. p. 147-177.

50. Vannice, M.A., *Kinetics of Catalytic Reactions*. 2005: Springer.

51. et.al., R., *Reommendations for the characterization of porous solids*. Vol. 66. 1994, Pure & Appl. Chem.

52. Riaz Qadeer, S.I. *Cobalt Impregnated Alumina: Nitrogen Adsorption Study at 77 K*. Turk J Chem 2004; Available from: http://journals.tubitak.gov.tr/chem/issues/kim-05-29-1/kim-29-1-12-0405-16.pdf.

53. al., A.E.A.e. *The Effect of Metal Loading on the Adsorption Parameters of Carbon Dioxide on Coprecipitated Nickel-Alumina Catalysts*. 1996 [cited 2016 11. July]; Available from: http://journals.tubitak.gov.tr/chem/issues/kim-96-20-1/kim-20-1-12-95073.pdf.

*

54. Bet K. S. W. Sing, D.H.E., R. A. W. Haul, L. Moscou, R. A. Pierotti, J. Rouqu´erol, and T. Siemieniewska, *Reporting Physisorption Data for Gas/Solid Systems.* Pure and Applied Chemistry, 1985. **57**: p. 603–619.

55. R. E. Walpole, R.H.M., S. L. Myers, K. Ye, *Probability & Statistics for Engineers and Scientists*. Pearson.

10 APPENDICES

10.1 Incipient wetness impregnation (IWI) and calcination

Alumina powder (more specific?) was sieved through a sieve with a pore size of 150 µm onto a sieve with pore size of 53 µm, whereon an effort was made to sift out the smaller particles. The alumina grains should be as small as possible to yield as high surface area as possible. Due to actual solar reactor conditions, however, very fine grains should be avoided. Sifting by hand proved more efficient than by vibratory machine sieve. The powder was then calcined in ceramic bowls in a high temperature furnace overnight at 500 °C. This was done to remove any moist in the alumina pores and burn away potential impurities, but also to yield the wanted type of alumina.

The water uptake of the alumina powder was tested by adding water slowly while continuously stirring. Water was added until one could see a shimmering water surface that would not be absorbed anymore. This test was repeated seemingly successfully three times with various amounts of the alumina powder. An average value of 1.36 gram of water per gram of alumina powder was found, but decided to be lowered to 1.2. Since stirring after

*

liquid has been added and is absorbed is assumed to be the most critical step to attain a uniform distribution of metal particles in the support, no more effort was put into trying to find the perfectly optimal value.

The redox material was prepared by first weighting alumina in a ceramic bowl. Initially, varying amounts of iron (III) nitrate nonahydrate and cobalt (II) nitrate hexahydrate (producer, catalogue number perhaps) was weighted and mixed together with water. The ionic mixture was then poured carefully onto the alumina powder while continuously stirring. When all liquid seemed absorbed, the powder was poured into a glass reactor with a sample holder of quartz. The sample was then dried and calcined in a calcination oven in nitrogen atmosphere by a heating rate of 1 °C/min up to 300 °C, before maintaining this temperature for 16 hours. At high concentrations of metal loadings, the metal crystal compounds would not be solved at room temperature. In these cases, the crystals were melted in a furnace at 70 °C. The alumina support was also heated together with stirrer and container. The liquid seemed to be absorbed slower at high temperatures, resulting in a slurry. As the slurry cooled down while being constantly stirred, however, excess liquid appeared to be absorbed gradually.

10.2 Cycle program specifications

Non-isothermal Ar program

Num	Mode	Temp. °C	HR K/min	Acq.Rate pts/min	Duration hh:mm	P1:Ar	P2:--	PG:Ar
---	Start	30.0				30.0	0.0	25.0
1	Isothermal	30.0		12.50	00:20	30.0	0.0	25.0
2	Dynamic	1400.0	5.00	75.00	04:34	30.0	0.0	25.0
3	Isothermal	1400.0		4.18	00:10	30.0	0.0	25.0
---	Emergency	1420.0				0.0	0.0	25.0

Non-isothermal O2 program

Num	Mode	Temp. °C	HR K/min	Acq.Rate pts/min	Duration hh:mm	P1:O2	P2:--	PG:Ar
---	Start	30.0				0.0	0.0	25.0
1	Isothermal	30.0		12.50	00:20	30.0	0.0	25.0
2	Dynamic	1400.0	5.00	75.00	04:34	30.0	0.0	25.0
3	Isothermal	1400.0		25.00	00:10	30.0	0.0	25.0
---	Emergency	1420.0				0.0	0.0	25.0

Ar/air cycles

Num	Mode	Temp. °C	HR K/min	Acq.Rate pts/min	Duration hh:mm	P1:Ar	P2:N2/O2	PG:Ar
---	Start	30.0				0.0	0.0	25.0
1	Dynamic	1400.0	50.00	100.00	00:27	75.0	0.0	25.0
2	Isothermal	1400.0		4.18	01:00	75.0	0.0	25.0
3	Isothermal	1400.0		4.18	00:45	75.0	5.0	25.0
4	Isothermal	1400.0		20.00	00:01	150.0	0.0	25.0
5	Isothermal	1400.0		20.00	01:00	75.0	0.0	25.0
6	Isothermal	1400.0		20.00	00:45	75.0	5.0	25.0
7	Isothermal	1400.0		20.00	00:01	150.0	0.0	25.0
8	Isothermal	1400.0		20.00	01:00	75.0	0.0	25.0
9	Isothermal	1400.0		20.00	00:45	75.0	5.0	25.0
10	Isothermal	1400.0		20.00	00:01	150.0	0.0	25.0
11	Isothermal	1400.0		20.00	01:00	75.0	0.0	25.0
12	Isothermal	1400.0		20.00	00:45	75.0	5.0	25.0
13	Isothermal	1400.0		20.00	00:01	150.0	0.0	25.0
14	Isothermal	1400.0		20.00	01:00	75.0	0.0	25.0
15	Isothermal	1400.0		20.00	00:45	75.0	5.0	25.0
16	Isothermal	1400.0		20.00	00:01	150.0	0.0	25.0
17	Isothermal	1400.0		20.00	01:00	75.0	0.0	25.0
18	Isothermal	1400.0		20.00	00:45	75.0	5.0	25.0
---	Emergency	1420.0				0.0	0.0	25.0

Ar/CO2 cycles

Num	Mode	Temp. °C	HR K/min	Acq.Rate pts/min	Duration hh:mm	P1:Ar	P2:CO2	PG:Ar
---	Start	30.0				0.0	0.0	25.0
1	Dynamic	1400.0	50.00	600.00	00:27	25.0	0.0	25.0
2	Isothermal	1400.0		500.00	01:00	25.0	0.0	25.0
3	Isothermal	1400.0		500.00	01:00	0.0	25.0	25.0
4	Isothermal	1400.0		500.00	00:01	30.0	0.0	25.0
5	Isothermal	1400.0		500.00	01:00	25.0	0.0	25.0
6	Isothermal	1400.0		500.00	01:00	0.0	25.0	25.0
7	Isothermal	1400.0		500.00	00:01	30.0	0.0	25.0
8	Isothermal	1400.0		500.00	01:00	25.0	0.0	25.0
9	Isothermal	1400.0		500.00	01:00	0.0	25.0	25.0
10	Isothermal	1400.0		500.00	00:01	30.0	0.0	25.0

*

11	Isothermal	1400.0		500.00	01:00	25.0	0.0	25.0
12	Isothermal	1400.0		500.00	01:00	0.0	25.0	25.0
13	Isothermal	1400.0		500.00	00:01	30.0	0.0	25.0
14	Isothermal	1400.0		500.00	01:00	25.0	0.0	25.0
15	Isothermal	1400.0		500.00	01:00	0.0	25.0	25.0
16	Isothermal	1400.0		500.00	00:01	30.0	0.0	25.0
17	Isothermal	1400.0		600.00	01:00	25.0	0.0	25.0
18	Isothermal	1400.0		600.00	01:00	0.0	25.0	25.0
---	Emergency	1420.0				0.0	0.0	25.0

Ar/1%O2 cycles

Num	Mode	Temp. °C	HR K/min	Acq.Rate pts/min	Duration hh:mm	P1:Ar	P2:1O2Ar	PG:Ar
---	Start	30.0				0.0	0.0	25.0
1	Dynamic	1400.0	50.00	600.00	00:27	25.0	0.0	25.0
2	Isothermal	1400.0		500.00	01:00	25.0	0.0	25.0
3	Isothermal	1400.0		500.00	01:00	0.0	25.0	25.0
4	Isothermal	1400.0		500.00	00:02	30.0	25.0	25.0
5	Isothermal	1400.0		500.00	01:00	25.0	0.0	25.0
6	Isothermal	1400.0		500.00	01:00	0.0	25.0	25.0
7	Isothermal	1400.0		500.00	00:02	30.0	0.0	25.0
8	Isothermal	1400.0		500.00	01:00	25.0	0.0	25.0
9	Isothermal	1400.0		500.00	01:00	0.0	25.0	25.0
10	Isothermal	1400.0		500.00	00:02	30.0	0.0	25.0
11	Isothermal	1400.0		500.00	01:00	25.0	0.0	25.0
12	Isothermal	1400.0		500.00	01:00	0.0	25.0	25.0
13	Isothermal	1400.0		500.00	00:02	30.0	0.0	25.0
14	Isothermal	1400.0		500.00	01:00	25.0	0.0	25.0
15	Isothermal	1400.0		500.00	01:00	0.0	25.0	25.0
16	Isothermal	1400.0		500.00	00:02	30.0	0.0	25.0
17	Isothermal	1400.0		500.00	01:00	25.0	0.0	25.0
18	Isothermal	1400.0		500.00	01:00	0.0	25.0	25.0
---	Emergency	1420.0				0.0	0.0	25.0

1%O2/Ar cycles

Num	Mode	Temp. °C	HR K/min	Acq.Rate pts/min	Duration hh:mm	P1:Ar	P2:1O2Ar	PG:Ar
---	Start	30.0				0.0	0.0	25.0
1	Dynamic	1400.0	50.00	600.00	00:27	0.0	25.0	25.0
2	Isothermal	1400.0		500.00	01:00	0.0	25.0	25.0
3	Isothermal	1400.0		500.00	00:02	30.0	0.0	25.0
4	Isothermal	1400.0		500.00	01:00	25.0	0.0	25.0
5	Isothermal	1400.0		500.00	01:00	0.0	25.0	25.0
6	Isothermal	1400.0		500.00	00:02	30.0	0.0	25.0
7	Isothermal	1400.0		500.00	01:00	25.0	0.0	25.0
8	Isothermal	1400.0		500.00	01:00	0.0	25.0	25.0

9	Isothermal	1400.0	500.00	00:02	30.0	0.0	25.0
10	Isothermal	1400.0	500.00	01:00	25.0	0.0	25.0
11	Isothermal	1400.0	500.00	01:00	0.0	25.0	25.0
12	Isothermal	1400.0	500.00	00:02	30.0	0.0	25.0
13	Isothermal	1400.0	500.00	01:00	25.0	0.0	25.0
14	Isothermal	1400.0	500.00	01:00	0.0	25.0	25.0
15	Isothermal	1400.0	500.00	00:02	30.0	0.0	25.0
16	Isothermal	1400.0	500.00	01:00	25.0	0.0	25.0
17	Isothermal	1400.0	500.00	01:00	0.0	25.0	25.0

10.3 TGA combined plots

10.3.1 Correction programs (empty crucible)

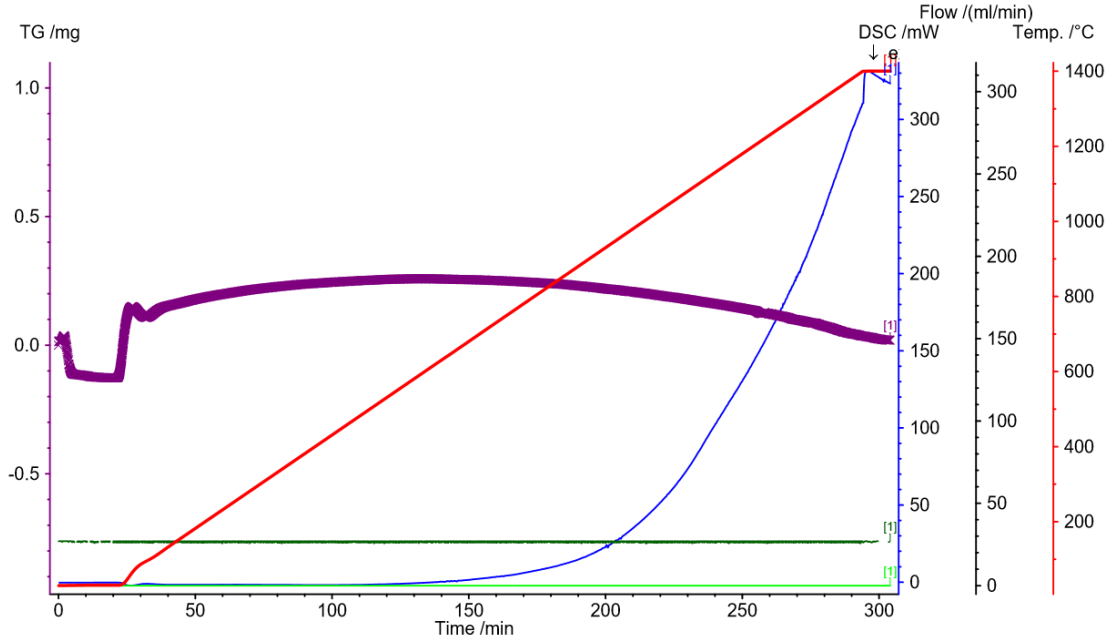

Figure 10.1: Non-isothermal Ar program

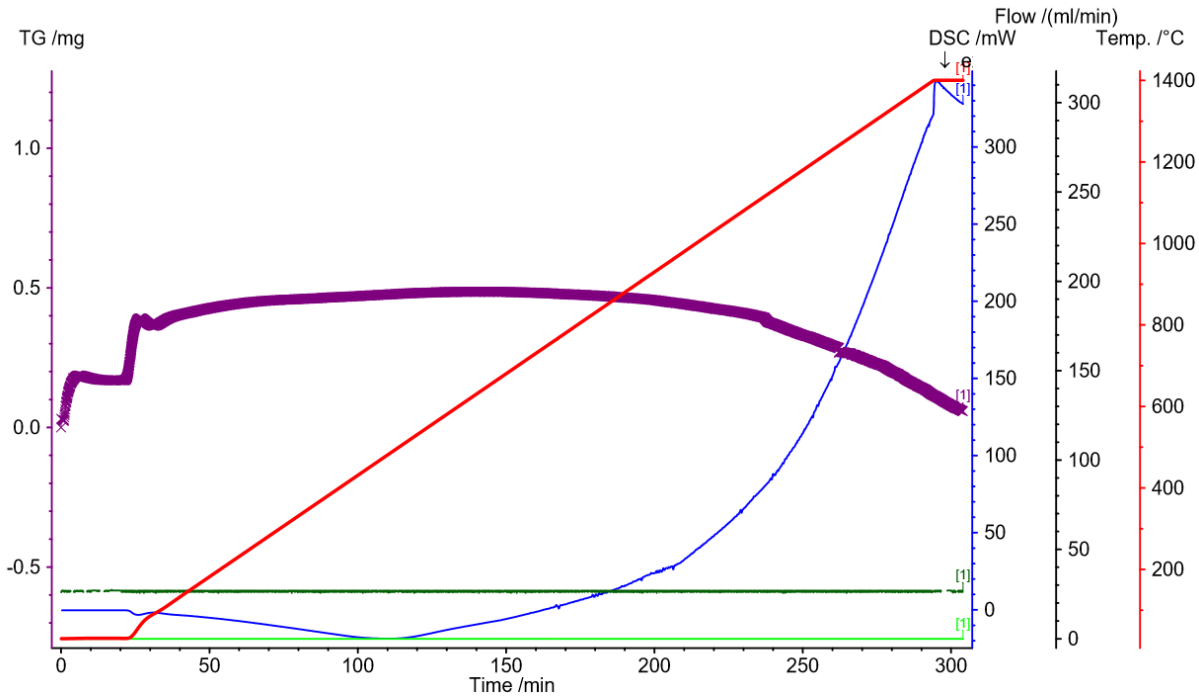

Figure 10.2: Non-isothermal O_2 program

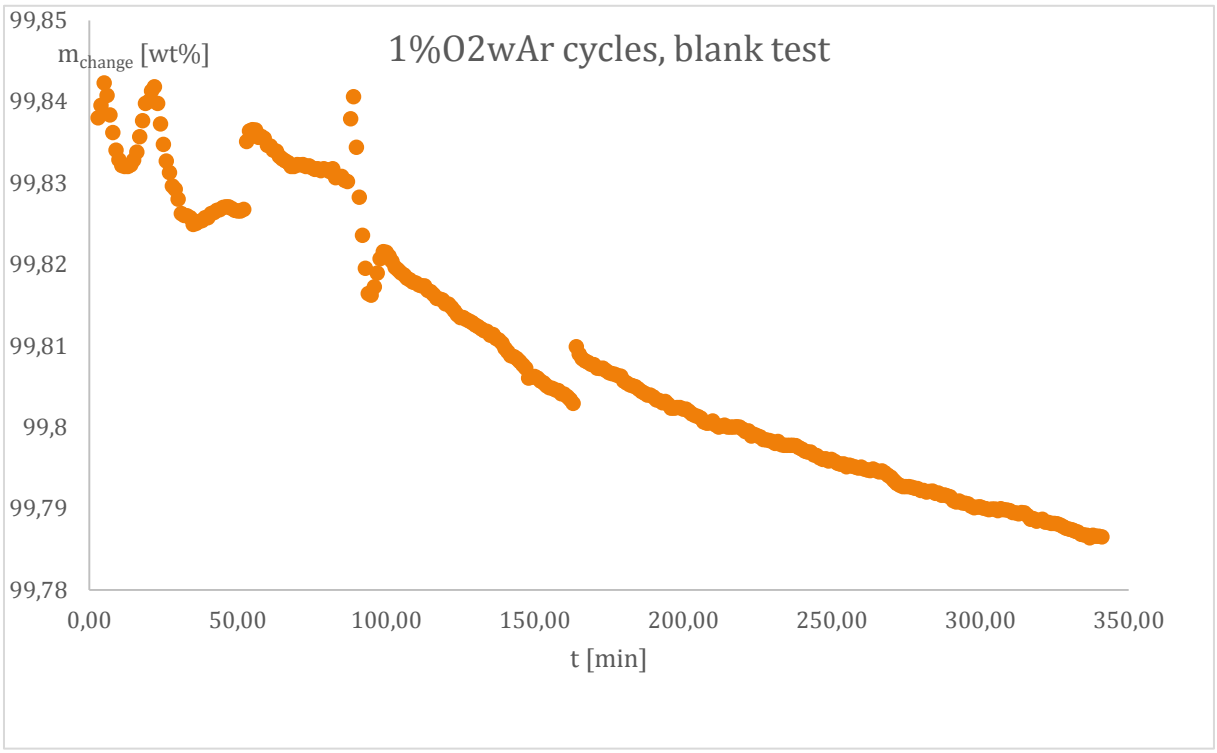

10.4 Selected MS signals

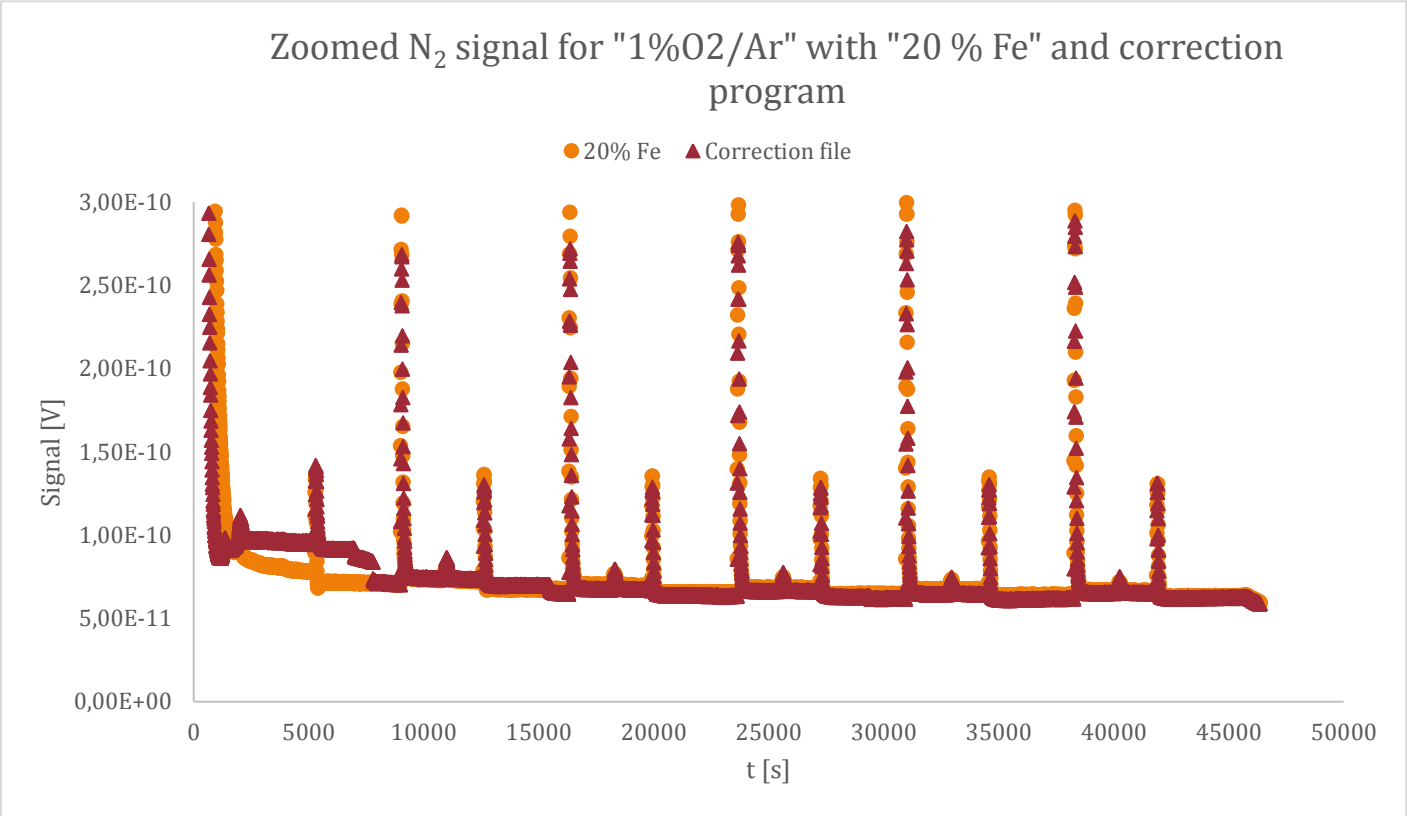

*

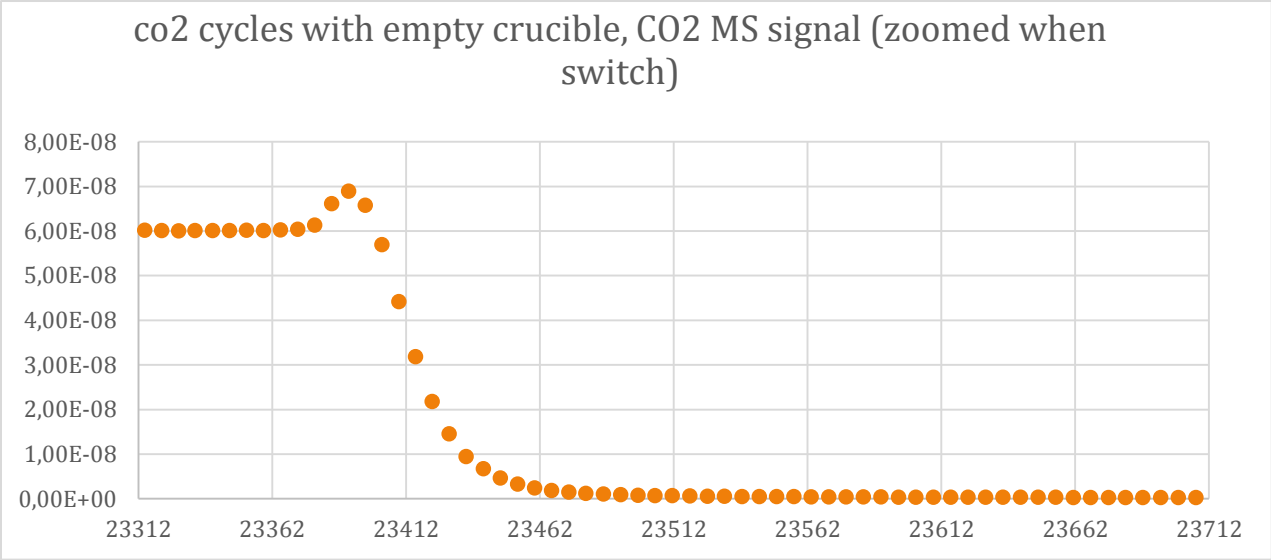

Time before CO2 is flushed away: 171 s = 2.85 min

10.5 Equivalent yield and uncertainty

The following formula was used for calculating theoretical yield:

$$\frac{N_{H_2}}{m_{dry\ sample}} = 2\frac{\%m_{change}}{\%m_{dry\ sample} \cdot M_{O_2}} \qquad (10.1)$$

Gauss' law of error propagation was used to calculate the uncertainty of the equivalent yield H_2 or CO. The standard deviation was first estimated for oxidation and reduction $\%m_{change}$ on the graphs, before the standard deviation formula in excel was used on all of these measured values to calculate the standard deviation of the data. Then, this value was divided on the square root of the number of measurements, in accordance with the Central Limit Theorem [55]. Next, the double standard deviation for $\%m_{dry\ sample}$ was assumed to be 0.50 %, while only $5 \cdot 10^{-5}$ g/mol for M_{O2}.

Parameters used:

Cycles	Sample	Assumed mass percent dry [wt%]	Max Fe content
O2 after Ar	20 % Fe (II)	99.400 %	17.94 %
Ar after 1 Ar/O2	20 % Fe (II)	100.00 %	17.94 %
		100 %	
6 Ar/air	10 % Fe	91.500 %	9.56 %
6 Ar/air	20 % Fe	94.00 %	17.96 %
6 Ar/air	20 % Fe (II)	93.500 %	17.94 %
6 Ar/air after 6 Ar/air	20 % Fe	98.00 %	17.96 %
6 Ar/CO2	10 % Fe	91.500 %	9.56 %
6 Ar/CO2	20 % Fe	92.00 %	17.96 %
6 Ar/CO2	20 % Fe (II)	92.500 %	17.94 %
6 Ar/1%O2	20 % Fe	90.300 %	17.96 %
6 1%O2/Ar	20 % Fe	89.400 %	17.96 %
5 1%O2/Ar	20 % Fe*	90.900 %	17.96 %

10.6 Weight percent of Fe in samples

It was assumed that Fe_2O_3 and CoO is transferred to the alumina when the active material was calculated. The purity of the precursor used was also taken into account. Since leaking is likely to occur during the initial calcination, the calculated one would be maximum wt% Fe.

All Fe content values are approximations based on reported values, except for Pechini where the materials were analyzed by ICP-OES with all molar ratios reported.

2014:

2014
The starting active material was synthesized to have a molar ratio Al2O3/CoFe2O4 = 3, but, with 15% excess Al2O3 in the matrix.

Assume N_al, inactive = 0.15*N_total

*

10.7 Derivative plots examples

The zoomed plot is for switching to reduction for the red values, and switching to oxidation for the blue values when using the special bottle. There is a similar shape of the empty space under the blue graph as reported by Weimer et. al. If assuming a peak rate of at least 0.1 %/min, one will get (0.1/(60*32*100%))*10^6 = 0.52 μmol O2/g_wet sample*s. But it seemed like the different plots varied too much.

Zoomed plot for Ar/1%O2 and 1%O2/Ar together during cycle switch:

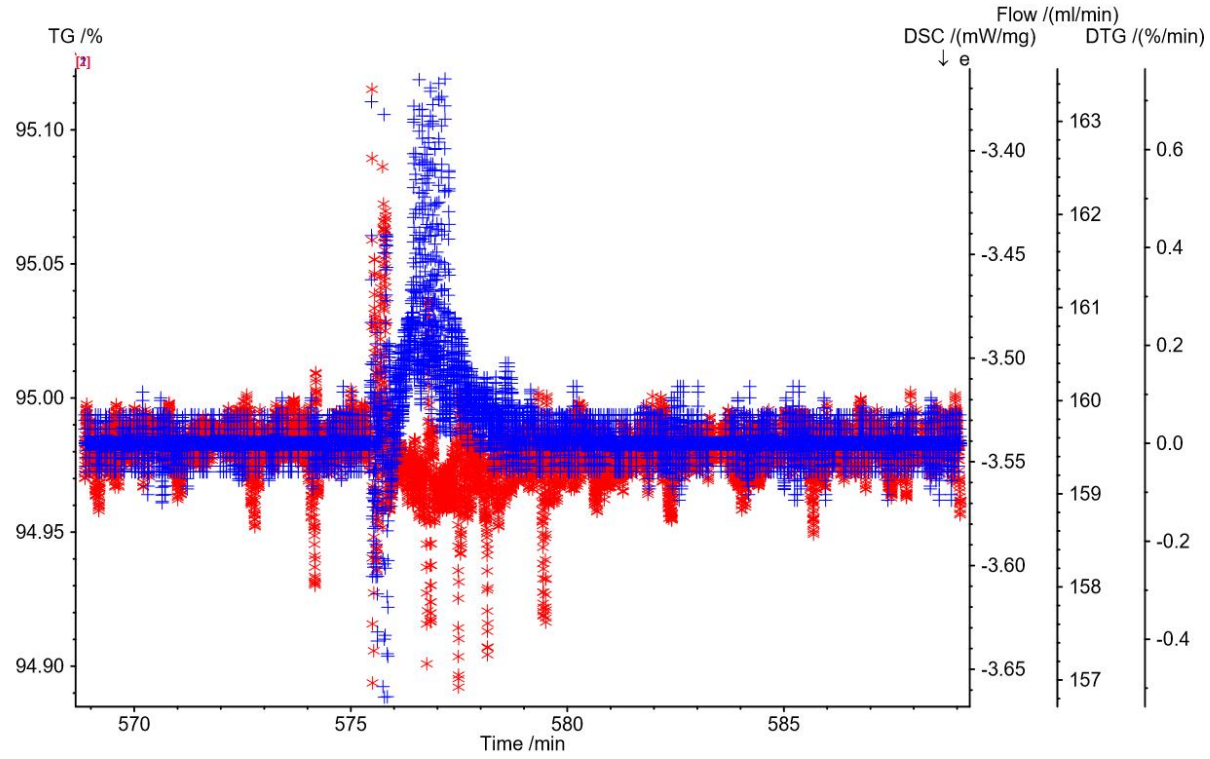

The pattern under the blue graph is somewhat similar to what has been reported earlier.

For 20%Fe, CO2 cycles, with derivative plot in pink:

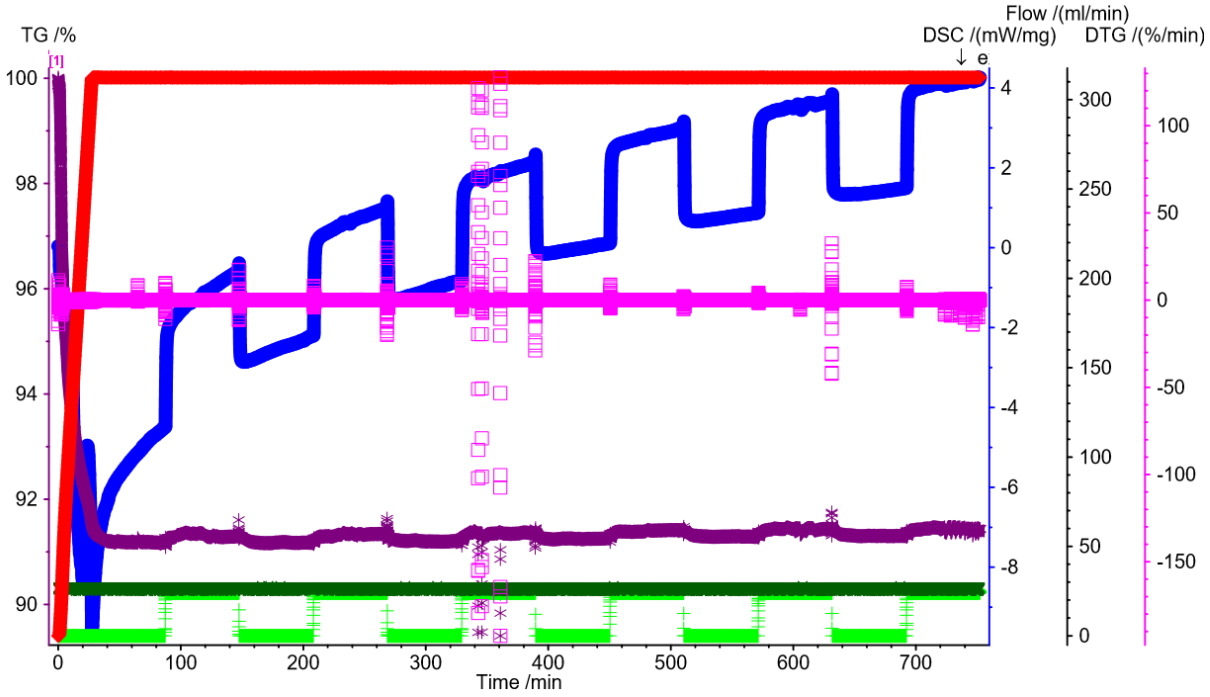

*

ID	5930	**Status**	**Dato**
Risikoområde	Risikovurdering: Helse, miljø og sikkerhet (HMS)	Opprettet	04.03.2016
Opprettet av	Tor Olav Høva Erevik	Vurdering startet	04.03.2016
Ansvarlig	Tor Olav Høva Erevik	Tiltak besluttet	
		Avsluttet	

Masteroppgave, ny vurdering

Gyldig i perioden:

1/15/2016 - 6/27/2019

Sted:

3 - Gløshaugen

Mål / hensikt

Klargjøre materialer ved insipientfuktingsteknikken; karakterisering innebefatter XRD og overflate-/poremålinger (BET). Testing vil skje ved minst en følgende metoder: Statisk kalsinering, TGA, in situ XRD eller fastsjiktsreaksjon.

Bakgrunn

Masteroppgave.

Beskrivelse og avgrensninger

Klargjøre og teste oksidkatalysatorer for bruk i termisk splitting av vann til hydrogen.

Forutsetninger, antakelser og forenklinger

Tilgjengelige relevante apparater ved institutt for materialteknologi og eventuelt hos Statoil.

Vedlegg

[Ingen registreringer]

Referanser

[Ingen registreringer]

Oppsummering, resultat og endelig vurdering

I oppsummeringen presenteres en oversikt over farer og uønskede hendelser, samt resultat for det enkelte konsekvensområdet.

Farekilde: **Utstyr og maskiner**

Uønsket hendelse: **Gasslekkasje**

Konsekvensområde:		
	Helse	Risiko før tiltak: Risiko etter tiltak:
	Materielle verdier	Risiko før tiltak: Risiko etter tiltak:
	Omdømme	Risiko før tiltak: Risiko etter tiltak:

Uønsket hendelse: **Ukontrollert oppvarming**

Konsekvensområde:		
	Helse	Risiko før tiltak: Risiko etter tiltak:
	Materielle verdier	Risiko før tiltak: Risiko etter tiltak:
	Omdømme	Risiko før tiltak: Risiko etter tiltak:

Uønsket hendelse: **Slitasje på utstyr**

Konsekvensområde:		
	Materielle verdier	Risiko før tiltak: Risiko etter tiltak:

Farekilde: **Stoffer**

Uønsket hendelse: **Skadelig kontakt**

Konsekvensområde:		
	Helse	Risiko før tiltak: Risiko etter tiltak:
	Omdømme	Risiko før tiltak: Risiko etter tiltak:

Uønsket hendelse: **Dårlig avfallshåndtering**

Konsekvensområde:		
	Helse	Risiko før tiltak: Risiko etter tiltak:
	Ytre miljø	Risiko før tiltak: Risiko etter tiltak:
	Omdømme	Risiko før tiltak: Risiko etter tiltak:

Uønsket hendelse: **Søl med flytende nitrogen**

Konsekvensområde:		
	Helse	Risiko før tiltak: Risiko etter tiltak:
	Materielle verdier	Risiko før tiltak: Risiko etter tiltak:
	Omdømme	Risiko før tiltak: Risiko etter tiltak:

Endelig vurdering

Oversikt involverte enheter og personell

En risikovurdering kan gjelde for en, eller flere enheter i organisasjonen. Denne oversikten presenterer involverte enheter og personell for gjeldende risikovurdering.

Enhet /-er risikovurderingen omfatter

- NTNU

Deltakere

[Ingen registreringer]

Lesere

[Ingen registreringer]

Andre involverte/interessenter

Veiledere; professor Magne Hillestad og professor Erling Rytter.

Følgende akseptkriterier er besluttet for risikoområdet Risikovurdering: Helse, miljø og sikkerhet (HMS):

Helse	Materielle verdier	Omdømme	Ytre miljø
			

Oversikt over eksisterende, relevante tiltak som er hensyntatt i risikovurderingen

I tabellen under presenteres eksisterende tiltak som er hensyntatt ved vurdering av sannsynlighet og konsekvens for aktuelle uønskede hendelser.

Farekilde	Uønsket hendelse	Tiltak hensyntatt ved vurdering
Utstyr og maskiner	Gasslekkasje	Opplæring
	Gasslekkasje	Håndmåler for CO-nivå
	Gasslekkasje	Alarmer for gasslekkasje og brann
	Ukontrollert oppvarming	Opplæring
	Slitasje på utstyr	Opplæring
Stoffer	Skadelig kontakt	Opplæring
	Skadelig kontakt	Verneutstyr
	Skadelig kontakt	Datablader, stoffkartotek, internett
	Skadelig kontakt	Avtrekkskap
	Skadelig kontakt	God avfallshåndtering
	Dårlig avfallshåndtering	Verneutstyr
	Dårlig avfallshåndtering	Avtrekkskap
	Dårlig avfallshåndtering	God avfallshåndtering
	Søl med flytende nitrogen	Opplæring
	Søl med flytende nitrogen	Verneutstyr
	Søl med flytende nitrogen	Alarmer for gasslekkasje og brann

Eksisterende og relevante tiltak med beskrivelse:

Opplæring
Opplæring om utstyr og verneinnretninger på laboratoriene.

Verneutstyr
Bruk av personlig verneutstyr, som labfrakk og vernebriller.

Datablader, stoffkartotek, internett
Oppsøke datablad, stoffkartotek eller internett for informasjon om eventuelle helsemessig risiko ved bruk av oksidene og andre stoffer som skal benyttes.

Koboltferritt i pulverform, som er et av stoffene som kanskje skal behandles, er helseskadelig og irriterende.

Avtrekkskap
Bruke avtrekkskap dersom oksidene som skal behandles utgjør noen helsemessig risiko.

God avfallshåndtering
Bruk av spesielle avfallsdunker og liknende.

Håndmåler for CO-nivå
[Ingen registreringer]

Alarmer for gasslekkasje og brann

[Ingen registreringer]

Risikoanalyse med vurdering av sannsynlighet og konsekvens

I denne delen av rapporten presenteres detaljer dokumentasjon av de farer, uønskede hendelser og årsaker som er vurdert. Innledningsvis oppsummeres farer med tilhørende uønskede hendelser som er tatt med i vurderingen.

Følgende farer og uønskede hendelser er vurdert i denne risikovurderingen:

- **Utstyr og maskiner**
  - Gasslekkasje
  - Ukontrollert oppvarming
  - Slitasje på utstyr
- **Stoffer**
  - Skadelig kontakt
  - Dårlig avfallshåndtering
  - Søl med flytende nitrogen

Oversikt over besluttede risikoreduserende tiltak med beskrivelse:

Utstyr og maskiner (farekilde)

Mennesker og materiell kan bli skadet dersom det skulle skje noe feil med apparatene.

Utstyr og maskiner/Gasslekkasje (uønsket hendelse)

Lekkasje av farlige NOx-gasser ved kalsinering av prøven under inert atmosfære.

Ukontrollert oppvarming og lekkasje av Ar, O2, CO2, CO, ved TGA.

Årsak: Apparatursvikt

Beskrivelse:

Det kan ha oppstått hull på slanger eller liknende for TGA eller kalsineringsovn.

Årsak: Menneskelig svikt

Beskrivelse:

Feilinnstilling av TGA / kalsineringsovn kan gjøre at systemet ikke blir helt tett. Flytende nitrogen kan bli sølt utover gulvet for BET.

Samlet sannsynlighet vurdert for hendelsen: Lite sannsynlig (2)

Kommentar til vurdering av sannsynlighet:

Apparaturfeil skjer som regel sjelden. Kontrollprosedyrer og varsomhet trekker også sannsynligheten ned.

Vurdering av risiko for følgende konsekvensområde: Helse

Vurdert sannsynlighet (felles for hendelsen): Lite sannsynlig (2)

Vurdert konsekvens: Svært stor (4)

Kommentar til vurdering av konsekvens:

Lekkasje av farlige NOx-gasser ved kalsinering av prøver under inert atmosfære kan være helseskadelig; det kan føre til kronisk redusert lungefunksjon og forverre eksisterende lunge- og hjertesykdommer. Svært høye konsentrasjoner kan være dødelig (>100 ppm). Kontrollverdi for NO er i følge sikkerhetsdatablad fra Sigma-Aldrich på kun 25 ppm. På det meste vil man ha ca 5 g nitrat i kalsineringsovnene om gangen. En liter luft veier ca. 1,2 g, og 1,3 kg for 1 m3. Så hvis man står med nesen kloss inntil en lekkasje, og NO2 utvikles raskt på dette tidspunktet, så kan det være dødelig. Dette er trolig lite sannsynlig siden reaksjonen sannsynligvis går over tid, og man har stor nok avstand til at gassen blir fortynnet.

Høye konsentrasjoner av NO2 kan forårsake eller forsterke brann; det er oksiderende og kan gi alvorlige etseskader på hud og øyne.

http://www.sigmaaldrich.com/MSDS/MSDS/PleaseWaitMSDSPage.do?language=&country=NO&brand=ALDRICH&productNumber=295566&PageToGoToURL=http%3A%2F%2Fwww.sigmaaldrich.com%2Fcatalog%2Fsearch%3Fterm%3Dnitrogen%2Bmonoxide%26interface%3DAll%26N%3D0%26mode%3Dpartialmax%26cm_re%3DDid%2520You%2520Mean-_-%26lang%3Den%26region%3DNO%26focus%3Dproduct%26cm_re%3DDid%2520You%2520Mean-_-

https://no.wikipedia.org/wiki/Nitrogenmonoksid_%E2%80%93_helseeffekter#Risikokarakterisering

https://en.wikipedia.org/wiki/Nitrogen_dioxide#Toxicity

Dersom store mengder flytende nitrogen søles ved BET, kan dette fordampe og fortrenge oksygen. Ved TGA kan lekkasje av argon og CO2 også fortrenge oksygen; kvelning.

Det antas å kunne dannes maksimalt 0,3 g CO i prøvekammeret ved TGA under reaksjon. Dette vil tilsvare ca. 200 ppm for en kubikkmeter med luft (alarmverdi er 100 ppm) dersom alt utvikles på en gang. Det er ventet at reaksjonen vil skje relativt raskt, så faren er reell. CO er meget giftig, og brannfarlig.

http://www.sigmaaldrich.com/MSDS/MSDS/DisplayMSDSPage.do?country=NO&language=no&productNumber=388505&brand=ALDRICH&PageToGoToURL=http%3A%2F%2Fwww.sigmaaldrich.com%2Fcatalog%2Fsearch%3Fterm%3Dcarbonmonoxide%26interface%3DAll%26N%3D0%26mode%3Dmatch%2520partialmax%26lang%3Den%26region%3DNO%26focus%3Dproduct

http://www.cpsc.gov/en/Safety-Education/Safety-Education-Centers/Carbon-Monoxide-Information-Center/Carbon-Monoxide-Questions-and-Answers-/

Lekkasje av oksygen kan øke brann- og eksplosjonsfaren.

Utstyr og maskiner/Ukontrollert oppvarming (uønsket hendelse)

Bruk av høytemperatursovner opp mot 1200 °C og kalsineringsovner opp mot 300 °C

Bruk av TGA opp mot 1400 °C

Årsak: Apparatursvikt

Beskrivelse:

Bruk av høytemperatursovner opp mot 1200 °C og kalsineringsovner opp mot 300 °C.
En maskinfeil kan f.eks. føre til ukontrollert oppvarming.

Årsak: Menneskelig svikt

Beskrivelse:

En person kan ved en feiltagelse åpne døren på veldig høy temperatur

Samlet sannsynlighet vurdert for hendelsen: Lite sannsynlig (2)

Kommentar til vurdering av sannsynlighet:

Apparaturfeil skjer som regel sjelden. Kontrollprosedyrer og varsomhet trekker også sannsynligheten ned.

Vurdering av risiko for følgende konsekvensområde: Helse

Vurdert sannsynlighet (felles for hendelsen): Lite sannsynlig (2)

Vurdert konsekvens: Stor (3)

Kommentar til vurdering av konsekvens:

Brannskader, ukontrollert oppvarming, brann. Branndetektorer og mulighet til å komme seg unna fort idet hendelsen starter gjør konsekvensene mindre alvorlig.

Utstyr og maskiner/Slitasje på utstyr (uønsket hendelse)

Årsak: Ukontrollert oppvarming

Beskrivelse:

Årsak: Gasstrykk i system

Beskrivelse:

For høyt eller lavt gasstrykk i deler av system på TGA

Samlet sannsynlighet vurdert for hendelsen: Lite sannsynlig (2)

Kommentar til vurdering av sannsynlighet:

Apparaturfeil skjer som regel sjelden. Kontrollprosedyrer og varsomhet trekker også sannsynligheten ned.

Vurdering av risiko for følgende konsekvensområde: Materielle verdier

Vurdert sannsynlighet (felles for hendelsen): Lite sannsynlig (2)

Vurdert konsekvens: Stor (3)

Kommentar til vurdering av konsekvens:

Apparaturen som benyttes er meget dyr.

Stoffer (farekilde)

Koboltferitt eller andre oksider eller stoffer.

Stoffer/Skadelig kontakt (uønsket hendelse)

Man kommer i direkte kontakt med stoffene på en skadelig måte, ved for eksempel innånding av aerosol eller overført til munn eller øyne ved at partikler fester seg på hendene.

Årsak: Mangelfull forberedelse

Beskrivelse:

Årsak: Mangelfull bruk av verneutstyr

Beskrivelse:

Årsak: Mangelfull bruk av avtrekkskap

Beskrivelse:

Samlet sannsynlighet vurdert for hendelsen: Lite sannsynlig (2)

Kommentar til vurdering av sannsynlighet:

Eksisterende tiltak regnes som tilstrekkelige.

Vurdering av risiko for følgende konsekvensområde: Helse

Vurdert sannsynlighet (felles for hendelsen): Lite sannsynlig (2)

Vurdert konsekvens: Svært stor (4)

Kommentar til vurdering av konsekvens:

Koboltnitratheksahydrat:

H272 Kan forsterke brann; oksiderende.
H302 Farlig ved svelging.
H317 Kan utløse en allergisk hudreaksjon.
H334 Kan gi allergi eller astmasymptomer eller pustevansker ved innånding.
H341 Mistenkes for å kunne forårsake genetiske skader.
H350i Kan forårsake kreft ved innånding.
H360F Kan skade forplantningsevnen.
H410 Meget giftig, med langtidsvirkning, for liv i vann.

http://www.sigmaaldrich.com/MSDS/MSDS/DisplayMSDSPage.do?country=NO&language=no&productNumber=239267&brand=SIAL&PageToGoToURL=http%3A%2F%2Fwww.sigmaaldrich.com%2Fcatalog%2Fsearch%3Fterm%3Dcobalt%2Bhexahydrate%2Bnitrate%26interface%3DAll%26N%3D0%26mode%3Dmatch%2520partialmax%26lang%3Den%26region%3DNO%26focus%3Dproduct

Jernnitratnonahydrat:

H314 Gir alvorlige etseskader på hud og øyne.

http://www.sigmaaldrich.com/MSDS/MSDS/DisplayMSDSPage.do?country=NO&language=no&productNumber=216828&brand=SIAL&PageToGoToURL=http%3A%2F%2Fwww.sigmaaldrich.com%2Fcatalog%2Fsearch%3Fterm%3DIron%2528III%2529%2BNitrate%2BNonahydrate%26interface%3DAll%26N%3D0%26mode%3Dmatch%2520partialmax%26lang%3Den%26region%3DNO%26focus%3Dproduct

Stoffer/Dårlig avfallshåndtering (uønsket hendelse)

Avfallstoffer blir ikke avhendet på en forsvarlig måte, slik som i spesielle avfallsdunker eller liknende.

Årsak: Dårlig avfallshåndtering

Beskrivelse:

Samlet sannsynlighet vurdert for hendelsen: Lite sannsynlig (2)

Kommentar til vurdering av sannsynlighet:

God avfallshåndtering

Vurdering av risiko for følgende konsekvensområde: Helse

Vurdert sannsynlighet (felles for hendelsen): Lite sannsynlig (2)

Vurdert konsekvens: Stor (3)

Kommentar til vurdering av konsekvens:

Koboltnitratheksahydrat:

H272 Kan forsterke brann; oksiderende.
H302 Farlig ved svelging.
H317 Kan utløse en allergisk hudreaksjon.
H334 Kan gi allergi eller astmasymptomer eller pustevansker ved innånding.
H341 Mistenkes for å kunne forårsake genetiske skader.
H350i Kan forårsake kreft ved innånding.
H360F Kan skade forplantningsevnen.
H410 Meget giftig, med langtidsvirkning, for liv i vann.

http://www.sigmaaldrich.com/MSDS/MSDS/DisplayMSDSPage.do?country=NO&language=no&productNumber=239267&brand=SIAL&PageToGoToURL=http%3A%2F%2Fwww.sigmaaldrich.com%2Fcatalog%2Fsearch%3Fterm%3Dcobalt%2Bhexahydrate%2Bnitrate%26interface%3DAll%26N%3D0%26mode%3Dmatch%2520partialmax%26lang%3Den%26region%3DNO%26focus%3Dproduct

Jernnitratnonahydrat:

H314 Gir alvorlige etseskader på hud og øyne.

http://www.sigmaaldrich.com/MSDS/MSDS/DisplayMSDSPage.do?country=NO&language=no&productNumber=216828&brand=SIAL&PageToGoToURL=http%3A%2F%2Fwww.sigmaaldrich.com%2Fcatalog%2Fsearch%3Fterm%3DIron%2528III%2529%2BNitrate%2BNonahydrate%26interface%3DAll%26N%3D0%26mode%3Dmatch%2520partialmax%26lang%3Den%26region%3DNO%26focus%3Dproduct

Stoffer/Søl med flytende nitrogen (uønsket hendelse)

Søl med flytende nitrogen på BET-laboratoriet.

Årsak: Menneskelig svikt

Beskrivelse:

Uhell kan forekomme.

Samlet sannsynlighet vurdert for hendelsen: Lite sannsynlig (2)

Kommentar til vurdering av sannsynlighet:

Varsomhet.

Vurdering av risiko for følgende konsekvensområde: Helse

Vurdert sannsynlighet (felles for hendelsen): Lite sannsynlig (2)

Vurdert konsekvens: Stor (3)

Kommentar til vurdering av konsekvens:

Frostskader. Mye søl kan føre til at fordampet nitrogen fortrenger oksygenet i luften.

Oversikt over besluttede risikoreduserende tiltak:

Under presenteres en oversikt over risikoreduserende tiltak som skal bidra til å reduseres sannsynlighet og/eller konsekvens for uønskede hendelser.

Oversikt over besluttede risikoreduserende tiltak med beskrivelse: